Stony Brook University

Understanding Nitrogen Uptake in the Rhizosphere of a Mycorrhizal Fungus and Plant

System

A Dissertation Presented

by

Tiffany Whitney Victor

to

The Graduate School

in Partial Fulfillment of the

Requirements

for the Degree of

Doctor of Philosophy

in

Chemistry

Stony Brook University

January 2018

Stony Brook University

The Graduate School

Tiffany Whitney Victor

We, the dissertation committee for the above candidate for the

Doctor of Philosophy degree, hereby recommend

acceptance of this dissertation.

Lisa M. Miller, Ph.D. -Dissertation Advisor
Affiliated Associate Professor, Department of Chemistry

Elizabeth Boon, Ph.D. - Chairperson of Defense
Associate Professor, Department of Chemistry

Jarrod B. French, Ph.D. - Third Member of Defense Committee
Assistant Professor, Department of Chemistry

Ryan Tappero, Ph.D. - Outside Member of Defense Committee
Chemist, National Synchrotron Light Source II, Brookhaven National Laboratory

This dissertation is accepted by the Graduate School

Charles Taber

Dean of the Graduate School

Abstract of the Dissertation

Understanding Nitrogen Uptake in the Rhizosphere of a Mycorrhizal Fungus and Plant

System

by

Tiffany Whitney Victor

Doctor of Philosophy

in

Chemistry

Stony Brook University

2018

The mechanistic links between plants and growth promoting micro-organisms in an eco-system involved in the production of biomass are currently very poorly understood. Observing the nutrient changes in the rhizosphere is a key step to understanding the molecular dynamics involved in these symbiotic interactions and nutrient pathways that facilitate plant growth. To study such a nutrient flow, a new application of Fourier Transform Infrared Imaging (FTIRI) was developed that entailed growing *Populus tremuloides* seedlings on a thin, nutrient-enriched Phytagel matrix that allows pixel to pixel measurement of the distribution of nutrients, in particular, nitrate and ammonium and sucrose added as a carbon source in the rhizosphere. For quantification of the nitrate concentration in the rhizosphere of experimental plants, a calibration curve was generated that gave the nitrate concentration at each pixel in the measured chemical images. The chemical images collected from the poplar rhizosphere showed a higher nitrate concentration present in regions where the fungus, *Laccaria bicolor,* was detected suggesting sequestration from the media toward the plant root. In the control experiments without *Laccaria*

bicolor, the nitrate concentration remains mostly constant while the experiments with the fungus indicate varying gradients in the nitrate concentration. These gradients may facilitate the uptake and transport of nitrate across the fungi to the plant. To study the proteins involved in the nitrogen transport in this symbiotic relationship, x-ray fluorescence microscopy was utilized to measure proteins tagged with lanthanide-binding tags (LBTs), which are GFP-like analogs of minimal size. LBTs are short peptide sequences comprised of 15-20 naturally occurring amino acids that bind trivalent lanthanide ions with a nano-molar affinity. Two and three-dimensional x-ray images revealed that this method is suitable for identifying single proteins. This ability to monitor nutrient changes with other micro-organisms in the rhizosphere and the proteins responsible for the nutrient transport are key steps to understanding these symbiotic associations which facilitate plant growth which can provide useful information for growing plants sustainably by taking advantage of already existing plant-microbe relationships.

To my dad, Felicien Victor, and my brothers, Ashley and Shemark.

Table of Contents

LIST OF FIGURES

LIST OF TABLES

LIST OF ABBREVIATIONS

AMTs	Ammonium Transporter System
BNP	Bionanoprobe
Ca	Calcium
Cl	Chlorine
dLBT	Double Lanthanide Binding Tag
ECM	Ectomycorrhizal
Er	Erbium
ERM	Extraradical Mycelium
Eu	Europium
Fe	Iron
FTIR	Fourier Transform Infrared
FTIRI	Fourier Transform Infrared Imaging
GFP	Green Fluorescent Protein
HATs	High Affinity Transport System
HXN	Hard X-ray Nanoprobe
IR	Infrared
IRM	Intraradical Mycelium
La	Lanthanide
LATs	Low Affinity Transport System
LBT	Lanthanide Binding Tag
Ln	Lanthanide

MCT	Mercury Cadmium Telluride
MLL	Multilayer Laue Lens
N	Nitrogen
NH_4^+	Ammonium
NO_3^-	Nitrate
NRTs	Nitrate Transporter System
NUE	Nitrogen Use Efficiency
OmpA	Outer Membrane Protein A
PGPB	Plant Growth Promoting Bacteria
PLS	Partial Least Squares
PLSR	Partial Least Squares Regression
RMSECV	Root Mean Square Error of Cross Validation
RMSEP	Root Mean Square Error of Prediction
RPD	Ratio of performance to Deviation
RSA	Root Structural Architecture
TEM	Transmission Electron Microscopy
Tr	Terbium
WPM	Woody Plant Medium
XFM	X-ray Fluorescence Microscopy
XRF	X-ray Fluorescence
YFP	Yellow Fluorescent Protein
Zn	Zinc

ACKNOWLEDGMENTS

Firstly, I would like to express my heartfelt gratitude to my advisor Dr. Lisa Miller for the continuous support of my research. Her guidance, expertise and encouragement have been instrumental in the completion of this thesis. Her training and passion for science have inspired me to pursue a career in scientific research.

Besides my adviser, I thank my colleagues at Brookhaven National Laboratory, Vito Graziano and Randy Smith for their constant support, training and assistance with laboratory equipment.

My sincere thanks goes to Dr. Yong Chu and the Hard X-ray Nanoprobe team at NSLS II for their assistance and expertise with the tomography experiments. Without their support, it would not be possible to conduct these experiments.

Finally, I thank my family and friends who have always encouraged and supported me, especially throughout this journey. To Noelita (mom), Keisha (sister) and Grace (best friend), thank you for always motivating me. To the rest of my friends (Khala, Upasana, Coray, Pratik, Koushik, Luisa and David) that have made this journey full of adventure, thank you.

CHAPTER 1

INTRODUCTION

1.1 CHALLENGES IN USING CHEMICAL FERTILIZERS TO GROW CROPS ON A LARGE SCALE

Broad scale cropping is an important source of our livelihood but its current and future production is at risk due to the financial and environmental costs associated with chemical fertilizers used on a large scale. Sustainable and cost-effective practices are therefore required to overcome these challenges amid the growing global warming crisis. Chemical fertilizers have become essential components of modern agriculture because they provide essential plant nutrients such as nitrogen, phosphorus and potassium. Currently, chemical fertilizers are sourced from mined ores or industrially produced through energy intensive processes [3]. It is estimated that in the next 20 years, the cost of using macro nutrients like phosphorus to supplement soils from mined ores will exceed the value yield, especially because phosphate rock is a finite source [3].

The overuse of chemical fertilizers causes detrimental environmental impacts including substantial pollution of soil, air and water and causes deleterious effects on soil microorganisms which affects the fertility status of soil [4]. Furthermore, threats including droughts, floods, increase in CO_2 levels and temperature posed by emerging climate change or global warming on soil systems makes the two aforementioned problems more problematic moving forward [5] [6].

1.2 BIO-FERTILIZERS

Beneficial soil organisms, like mycorrhizal fungi and plant growth promoting bacteria (PGPB) that exist in soils can be used as bio-fertilizers as an alternative to chemical fertilizers providing nutrients to plants, improving plant growth and enhancing crop production, all while doing so sustainably. Growing crops with growth promoting micro-organisms would reduce the dependence on high levels of chemical fertilizers in the soil [3], reduce the harmful environmental effects of chemical fertilizers and help to cope with increasing levels of CO_2 [7].

Plant growth promoting bacteria improve the nutrient turnover in soils making it more fertile through a variety of mechanisms that involve decomposition of organic matter, recycling of essential elements, solubilization of mineral nutrients, producing numerous plant growth regulators which stimulate root growth, degrading organic pollutants and eliminating plant pathogens [4]. Mycorrhizal fungi increase plant growth by foraging the soil to find the necessary nutrients for its host plant and converts the nutrients in the correct chemical form before transferring the nutrients to the host plant [8, 9]. Additionally, these symbiotic fungi enhance plant protection against pathogens in the soil [10]. Although there have been many advances in understanding the molecular mechanisms of these symbiotic relationships, the current knowledge gap hinders the use of plant growth promoting bacteria and mycorrhizal fungi as bio-fertilizers on large industrial scales.

An understanding of their interactions from the molecular to the community level would enable a more effective use of these bio-fertilizers, which could also be used in bioremediation applications, energy generation processes, and in biotechnological industries such as pharmaceuticals, food, chemicals, and mining [11]. These bio-fertilizers would not only reduce

chemical fertilizer application economically, but provide environmental benefits by using the best soil and crop management practices to achieve more sustainable agriculture.

1.3 RENEWABLE BIOMASS FOR BIOFUEL PRODUCTION

The increasing consumption of energy, limited availability of fossil fuels, and environmental pollution from exhaust emissions have created a great demand for biofuels that can be produced from renewable biomass [12]. Biomass is the plant material derived from the reaction between CO_2 in the air, water and sunlight, via photosynthesis, to produce carbohydrates that form the building blocks of biomass [13]. If biomass is processed efficiently through the extraction of the energy stored in the chemical bonds of the `energy' product combined with oxygen, then carbon is oxidized to produce CO_2 and water; the process is cyclical, as the CO_2 is then available to produce new biomass [13].

Biofuels that have been presented as alternatives to petroleum based fuels are continuously critiqued on their availability and use on fertile lands that could serve for food production [14]. This presents a need to not only generate more biomass, but to do so on marginal, nutrient depleted lands. Soil microorganisms are a potentially important resource for enhancing biofuel production at a lower cost while maintaining ecosystem services. Their benefits can include nitrogen fixation, enhanced nutrient recycling and acquisition, production of growth stimulants, improved soil structure and water retention, and suppression of root diseases [15].

1.4 THE RHIZOSPHERE

In 1904, the German agronomist and plant physiologist Lorenz Hiltner first coined the term "rhizosphere" to describe the soil-root interface [16]. He described the rhizosphere (**Figure 1-1**) as the area around a plant root that is inhabited by a unique population of microorganisms influenced by the chemicals released from plant roots. The rhizosphere extends from 2 to 80 mm from the plant surface depending on the plant species [17]. Due to the inherent complexity and diversity of plant root systems, the rhizosphere is not a region of definable size or shape, but instead, consists of a gradient in chemical, biological and physical properties which change both radially and longitudinally along the root. The rhizosphere's microbial population promotes plant growth and health by breaking down organic matter, mineralizing nutrients, fixing nitrogen, and providing protection from pests and pathogens [18]. The plant species and root zone can also affect the structural and functional diversity of the rhizosphere microbial community due to variations in root exudation and rhizodeposition in different zones [19].
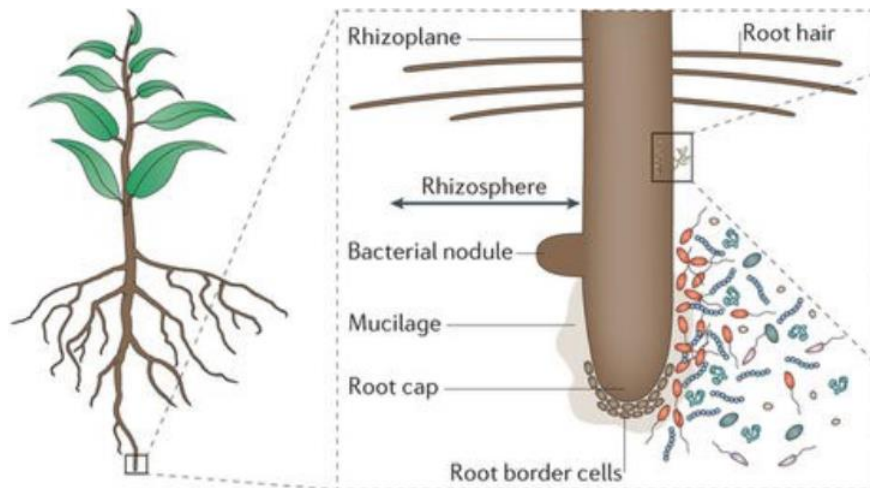
Figure 1-1: The rhizosphere. The rhizosphere is a narrow region of soil that is most actively involved in nutrient uptake processes. Figure adapted from [1].

1.5 MICROBIAL ECOLOGY OF THE RHIZOSPHERE

Both fungi and bacteria have been shown to promote plant growth through symbiosis [16].

1.5.1 THE MYCORRHIZA

Mycorrhiza is a general term describing the symbiotic relationship between a soil fungus and plant root. There are two broad categories of mycorrhizal associations (**Figure 1-2**) with plant roots, ectomycorrhiza (ECM) and endomycorrhiza (or arbuscular mycorrhiza), which are differentiated by how the fungus physically associates with the plant. Multicellular fungi are microscopic cells that grow as thin, long strands called hyphae that are only a few microns in diameter. When these hyphal strands are grouped into masses, they are called mycelium or thick, cord like 'rizomorphs' that look like roots [20]. Ectomycorrhiza form hyphae which grow into the intercellular spaces of the plant forming a net of hyphae around the root cortex cells, but do not penetrate the cell walls. In contrast, the endomycorrhiza fungal hyphae grow into the root cortex and enter the cells forming fan-like, highly branched structures. The morphology of mycorrhizal roots is known to be dramatically different from that of non-mycorrhizal roots. In preparation for root symbiosis, ECM roots undergo several changes including the inhibition of root hair formation, production of several meristem and extensive dichotomous branching of roots [21] [22].

The ectomycorrhiza (EM) occur mainly in the roots of woody plants and comprise of three main components; the hyphal sheath or mantle, the Hartig net also referred to as the intraradical mycelium (IRM) and the extraradical mycelium (ECM). Each of these three structural components plays an important role in facilitating the mycorrhizal relationship. The

ECM forms an extension of the root system and is the nutrient absorbing surface, forming 99% of the nutrient absorbing length in some plants [21]. In fungi like *L. bicolor*, the ECM forms several singular hyphae, as well as rhizomorphs which are aggregates of hyphae. The fungal sheath is responsible for nutrient storage and controls nutrient transfer to the plant while the Hartig net transfers nutrients between both plant and fungus [21]. The hyphal sheath forms a thick and rough multi-layer over the plant root with several hyphal strands extending from it while the Hartig net is comprised of hyphae that weaves into the root cortex intercellularly.
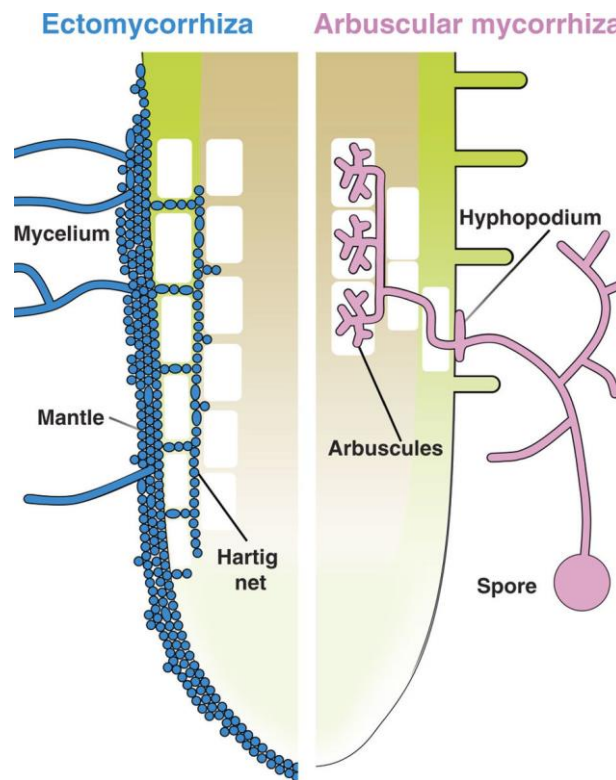
Figure 1-2: Types of Mycorrhizal Fungi. The ectomycorrhizal fungus surrounds the root tip with a thick mantle of closely associated hyphae, whereas the Hartig net develops around epidermal cells (green). In the case of arbuscular mycorrhizas, the root tip is usually not colonized. Intraradical colonization proceeds both intra and intercellularly and culminates with the formation of arbuscules, little fungal trees, inside inner cortical cells (brown)[2].

1.5.2 PLANT GROWTH PROMOTING BACTERIA

Plant growth-promoting bacteria (PGPB) are bacteria that can enhance plant growth and protect plants from diseases and abiotic stresses through a wide variety of direct and indirect mechanisms. PGPB, like *Pseudomonas fluorescens,* utilize mechanisms including nitrogen fixation, phosphate solubilization, iron chelation and phytohormone production [23, 24].

1.6 NITROGEN AS THE PRIMARY MACRONUTRIENT FOR PLANT GROWTH

Plants respond to changing environments and developmental factors by altering root structural architecture (RSA), recruiting the help of microorganisms and manipulating its nutrient transporter system. Signaling cascades control how much of a nutrient is acquired by the roots. Nitrogen, phosphorus, and sulfur are macronutrients that are required for plant growth and reproduction [25]. These elements are present in the soil as organic and inorganic forms, including the anionic species nitrate, phosphate, and sulfate [25]. Nitrogen, which is the primary macronutrient limiting plant growth [26], is required for the cellular synthesis of proteins including enzymes, chlorophyll, DNA and RNA, and is therefore important in leaf and root development, and production of food and feed [27]. Trees have different preferences for nitrogen sources that depend on the species and soil environment. Aspen seedlings can utilize both forms of inorganic nitrogen sources, either nitrate ($NO3^-$) or ammonium ($NH4^+$)[7]. Most organic nitrogen sources must be first broken down by proteolytic enzymes that originate from microbes or plant roots [7] while free amino acids can be readily absorbed by plant roots [28].

1.7 NITROGEN TRANSPORTERS IN PLANTS

The uptake of NO_3^- and NH_4^+ seems to be the result of influx and efflux proteins [7]. Studies in Populus tremuloides revealed high affinity transport systems (HATS) and low-affinity non-saturable transport systems (LATS). The HATS operate in the sub millimolar concentration range, less than 500 μM and the LATS operate in the millimolar concentration range [7]. Both nitrate transporters (NRTs) and ammonium transports (AMTs) have different affinity type proteins that are tissue specific and are produced under different conditions like mycorrhizal inoculation or senescence. The ammonium transporter, AMT1-2, is a highly expressed HAT protein in mycorrhizal roots while AMT3-1 is exclusively found in the shoots of some plants [7]. Unlike inorganic nitrogen transporters, amino acids are transported with one or two proteins via proton symporter mechanisms [7]. In ectomycorrhiza symbiosis, fungal and plant metabolisms are connected by a suite of transporters that shuttle essential nutrients across the apoplast from one organism to the other to form a combined system [4].

Nutrients are exchanged between fungi and roots across the apoplast, a zone outside both root and fungus, preventing direct contact between the fungi and plant cytoplasm and requiring that nutrients be exchanged cross both fungal and plant cell walls.

1.8 RESEARCH GAP

The mechanistic links within ecosystems involving plants, fungi, and soil bacteria involved in the production of biomass are currently very poorly defined. A detailed account of the transport mechanisms and sensor inputs will increase our understanding of the molecular connections between environmental components and cellular metabolic pathways and regulatory

networks. This information is essential to understanding the basis for occupancy of an ecological niche.

Because of the ecological significance and the application potential of mycorrhizal fungi as biofertilizers and phytoremediation components, it is important to understand the mechanism of the relationship with their host plant. At present, much is still unknown, for example: what molecules are involved in the crosstalk between mycorrhizal fungi and plants or how nutrients are acquired or transported to plants [29]. Additionally, it is unknown which genes are responsible for the establishment and maintenance of the mycorrhizal symbiosis. Furthermore, it has been challenging to image and make predictions of rhizosphere processes because of the inability to study such interactions in situ [30].

1.9 SPECIFIC AIMS

In this thesis, a unique experimental model system, comprised of plant, fungus, and bacteria, was used to examine the nutrient distribution in the rhizosphere under different nutrient conditions with the overreaching goal of gaining a broader understanding of the role of mycorrhizal fungi in nitrogen transport in the rhizosphere.

1.9.1 AIM 1: DEVELOP A METHOD FOR INFRARED IMAGING OF NUTRIENTS IN RHIZOSPHERE

To facilitate discrete characterization of the biological function of these critical proteins, a unique experimental model system comprised of *Populus tremuloides*, *Laccaria bicolor*, and *Pseudomonas fluorescens* was used to minimize system complexity and permit manipulation of nutrient parameters under controlled conditions. *To image the nitrate, ammonium and sucrose*

distribution in the rhizosphere, a FTIR-based imaging method was developed to capture the chemical state of the experimental model system.

1.9.2 AIM 2: ASSESS THE EFFECTS OF NUTRIENT DEPLETION IN THE PRESENCE AND ABSENCE OF BACTERIA/FUNGUS WITH POPLAR

The nutrient most limiting to plant growth is nitrogen due to the solubility of inorganic nitrogen sources and the inability of plants to utilize organic forms of nitrogen present in the soil. Microbes however, can convert and break down organic nitrogen sources for plant use and fungi can supply inorganic nitrogen that is inaccessible to the plant. *To better understand how inorganic nitrogen sources along with carbon sources are used within a community system, the effects of varying nutrient conditions on the model system were assessed using FTIR imaging.*

1.9.3 AIM 3: USE LANTHANIDE BINDING TAGS (LBTS) WITH X-RAY FLUORESCENCE MICROSCOPY (XFM) TO IMAGE INDIVIDUAL PROTEINS IN BACTERIA

Under low nutrient conditions in the soil, plants and symbiotic micro-organisms are quicker to form an association to make use of limited nutrient supplies. Under these conditions, transporter proteins involved in these symbiotic relationships become highly expressed. *To visualize the expression of these membrane proteins, a new application of lanthanide binding tags was developed for x-ray fluorescence microscopy in order to image individual transporter proteins in intact bacteria at the nanoscale.*

1.10 EXPERIMENTAL MODEL SYSTEM

To carry out this research project, a simple yet unique experimental system was developed to carry out the specific aims.

The community model system (**Figure 1-3**) comprised of a wooded plant species, (Quaking Aspen/poplar - *Populus Tremuolides), a fungus (Laccaria bicolor)*, and a soil bacteria (*Pseudomonas* fluorescens) which captures a diverse set of molecular responses derived from organisms that interact in natural ecosystems. All three of these organisms were cultured individually in rich or defined media, the latter enabling nutrient limitation studies. The experimental model system is grown in a transparent gel (phytagel) that plays the role of a transparent soil providing support and nutrients for the poplar system to grow [31]. It is through this faux-soil, that the poplar receives its macronutrients including nitrates and phosphates, and sucrose as a carbon source.

Figure 1-3: Experimental Model System shows poplar seedlings grown on glass slides in centrifuge tubes. Top row shows plants grown in control N media and bottom row shows plants grown in low N media. The image shows plant only **(A, E)**, plant + bacteria **(B, F)**, plant + fungus **(C, G)**, plant + fungus + bacteria **(D, H)**. The glass slide is coated with a gel matrix that provides nutrients for the plans. Extra liquid media is added to the bottom of the tube. The glass slide is 25 mm * 75 mm.

1.11 TECHNIQUES AND METHODS

1.11.1 FOURIER TRANSFORM INFRARED IMAGING (FTIRI)

FTIR-Imaging was used to obtain chemical snapshots of plants grown under different conditions to determine which growth condition optimizes nutrient transport in the rhizosphere. The combination of spectroscopy with imaging provides an exceptional technique for elucidating the nitrate and ammonium distribution in the rhizosphere at different spatial resolutions.

A molecule's stretching and bending movements are collectively referred to as its molecular vibrations. Infrared (IR) radiation can be absorbed by molecules when the frequency of radiation is equal to that of the natural frequencies at which the molecule vibrates. For a molecule to possess an infrared absorption, it must exhibit a change in electric dipole when the radiation is absorbed as in the case of C-H or C=O bonds. When the radiation is absorbed, a transition from one vibrational or rotational state to another occurs and is seen in the IR spectrum of a molecule.

FTIR-Imaging provides high spatially resolved chemical information to determine where specific events are happening. It is sensitive to simultaneous compositional changes without the use of added contrast agents [32] making it a valuable method for imaging the distribution of nutrients in the media under different conditions. The primary nutrients of concern in this research are nitrates and ammonium, and sucrose added as a carbon source. Using FTIR imaging provides a reliable way to spatially-resolve the vibrational bands of the different nutrients required for plant growth in the rhizosphere.

1.11.2 QUANTITATIVE PREDICTIVE MODELING USING PARTIAL LEAST SQUARES REGRESSION

1.11.2.1 THEORETICAL BACKGROUND

In a multicomponent sample with overlapping infrared peaks, it is difficult to assign infrared peaks to individual components making univariate analysis an unlikely choice for prediction of components. By incorporating multivariate regression approaches to the analysis of infrared spectroscopy from multicomponent samples, mathematical and statistical techniques were used to tease out hidden data. Partial least squares (PLS) regression is a statistical method used to find an approximate mathematical relationship between predictor and target variables such that the sum of squared errors between the true and predicted value is minimized. PLS regression predicts the property, Y, of a system from an experimentally observable X, whereby X and Y are calibrated by a function b.

$$Y = X*b \qquad\qquad (equation\ 1)$$

or

$$[y] = [spectrum]*b \qquad\qquad (equation\ 2)$$

The row vectors of the matrix X are from the calibration spectra and the Y vector consists of the component value. The aim is to determine the vector b that minimizes the sum of the error terms and is used to make predictions for unknown values of Y. The solution to the least squares problem is given by

$$b = (X^TX)^{-1}X^TY \qquad\qquad (equation\ 3)$$

Given that X is a *nxp* matrix and Y is a *nxq* matrix, the PLS technique works by iteratively extracting factors or scores from both X and Y such that the covariance between the extracted factors is maximized. The goal is to find a regression between the X scores and Y scores by linearly decomposing the matrices X and Y such that:

$$X = TP^T + E \text{ and } Y = UQ^T + F \qquad \text{(equation 4)}$$

The matrix, *X*, is decomposed into a matrix, *T* (referred to as *X*-score), and a matrix, *P′* (referred to as *X*-loading), plus an error matrix, *E*. The matrix, *Y*, is equivalently decomposed, into the *Y*-scores, *U*, the *Y*-loadings, *Q′*, and the error term, *F*. Once the first x and y score have been established, it is extracted from the matrix and the process continues until the matrix becomes null.

1.11.2.2 BUILDING A PREDICTIVE MODEL FROM INFRARED SPECTRA

To build a calibration model, several spectra of each sample need to be acquired to ensure reproducibility. Standard samples collected should span the range of expected outcomes. When more than one component is used to build the model, collinearity should be avoided to establish an independent calibration. By plotting one component value versus the other, a squared correlation coefficient can be determined. In general, spectral preprocessing is incorporated in building the model to remove deviations in features including deviations in linear baselines and offsets. To remove differences in sample thickness (path length of infrared light through the sample), normalization of the spectra was performed. Data preprocessing ensures a good correlation between the spectra and the assigned concentrations and the type of preprocessing used depends on individual samples.

1.11.2.3 VALIDATING THE MODEL

When a quantitative model is built, it has to be evaluated and its reliability of prediction has to be tested, i.e, validated. In this research, cross validation was employed to validate the model. In cross validation, one sample is excluded from the sample set and is used for validation. The remaining samples are used to calibrate the data. Once the calibration model is created, it is tested on the sample that was excluded. This cycle is repeated by excluding another sample, building the model again and testing the model on the newly excluded sample until all samples have been used for the validation once. The calibration set is a matrix of spectral data. This matrix is transformed using the PLS algorithm mentioned above to find a new resultant matrix containing factors (eigenvectors). Each factor has a different contribution to the spectral features and is listed in decreasing order of influence in the resultant matrix. Some factors, i.e those closer to the bottom of the matrix are not important to describe the spectral features and may only describe spectral noise. There is an optimum number of factors, also called rank, which gives the best representative model. The optimum rank is selected by plotting the root mean square error of prediction (RMSEP) versus the number of factors and selecting the number of factors with the minimum RMSEP.

1.11.3 X-RAY FLORESCENCE MICROSCOPY (XFM)

X-ray fluorescence microscopy (XFM) is a non-destructive analytical approach to determine the elemental composition of materials. In this thesis, it was used to show the distribution of elements, such as erbium, zinc and calcium in *E. coli* cells. Synchrotron-based X-ray fluorescence microscopy uses a spatially coherent and highly brilliant x-ray source that can

be focused to sub-micrometer probe size with advanced x-ray optics and is capable of detecting trace elements with a sensitivity down to parts per million (p.p.m.) in whole cells or tissue sections [33].

In XFM, hard X-rays are focused onto a specimen to induce characteristic x-ray fluorescence in the samples. When an atom within a sample is struck with a sufficient x-ray energy, an electron from the atom's inner shell orbital is dislodged and an electron from the higher energy, outer shell fills in the lost inner shell electron. This process releases x-ray fluorescence that accounts for the difference in energy between these two quantum states of the electron. Each element has characteristic x-ray fluorescence energies and a full energy dispersive spectrum can be acquired that shows all elements simultaneously. A graphical representation of x-ray fluorescence peak intensities as a function of energy shows what elements are present and the height indicates the intensity or concentration of the element present.

XFM data presented in this thesis were collected from two different XFM beamlines, the Bio-nanoprobe beamline (21-ID-E) at the Advanced Photon Source at the Argonne National Laboratory and the Hard X-ray Nanoprobe beamline (HXN) 3-ID beamline at the National Synchrotron Light Source II at Brookhaven National Laboratory. A typical XFM beamline is equipped with a monochromator, focusing optics, a moveable sample stage and a detector. At HXN, a new class of x-ray nanofocusing optics, known as multilayer Laue lenses (MLLs), is utilized to achieve high spatial resolutions of ~10-15 nm [34]. The BNP beamline uses Fresnel zone plate focusing optics to achieve a resolution of about 90 nm. Additionally, the BNP setup has the capability to collect data from samples under cryogenic conditions which is essential when studying biological samples in a frozen-hydrated state, which is close to its natural state.

1.11.3.1 X-RAY FLUORESCENCE TOMOGRAPHY

X-ray florescence tomography is a three-dimensional extension of 2D x-ray fluorescence microscopy (XFM). Tomography means 'slice imaging'. It uses the same principles as computed tomography, which involves reconstructing projections of an object viewed from different directions. By recording multiple images (projections) at different angles, a 3D reconstruction of the original sample is possible. The back-projection method used is based on inverting recorded images and projecting them back into the angle at which the original image was taken [35]. In principle, a higher number of projections at different angles gives a better reconstructed image. The chemical sensitivity that accompanies x-ray fluorescence nano-tomography makes it a powerful technique to image whole cells and tissues and is quite advantageous when deciphering exactly where elementals signals are located in samples which can be ambiguous in 2D XFM.

CHAPTER 2

IMAGING NUTRIENT DISTRIBUTION IN THE RHIZOSPHERE USING FTIR IMAGING

2.1 ABSTRACT

Symbiotic associations in the rhizosphere between plants and microorganisms lead to efficient changes in the distribution of nutrients that promote growth and development for each organism involved. Understanding these nutrient fluxes provides insight into the molecular dynamics involved in nutrient transport from one organism to the other. To study such nutrient flow, a new application of Fourier Transform Infrared Imaging (FTIRI) was developed that entailed growing *Populus tremuloides* seedlings on a thin, nutrient-enriched Phytagel matrix that allows pixel to pixel measurement of the distribution of nutrients – in particular nitrate – in the rhizosphere. The FTIR spectra collected from ammonium nitrate in the matrix indicated the greatest changes in the spectra at 1340 cm^{-1} due to the asymmetric stretching vibrations of nitrate. To quantify the nitrate concentration in the rhizosphere of experimental plants, a calibration curve was generated that gave the nitrate concentration at each pixel in the chemical image. These images of the poplar rhizosphere showed evidence for symbiotic sharing of nutrients between the plant and the fungi, *Laccaria bicolor,* where the nitrate concentration was five times higher near mycorrhizal roots than further out into the rhizosphere. This suggested that nitrates are acquired and transported from the media toward the plant root by the fungi. Similarly, the sucrose used in the growth media as a carbon source was depleted around the

fungi, suggesting its uptake and consumption by the system. This study is the first of its kind to visualize and quantify the nutrient availability associated with mycorrhizal interactions, indicating that FTIRI has the ability to monitor nutrient changes with other microorganisms in the rhizosphere as a key step for understanding nutrient flow processes in more diverse biological systems.

2.2 INTRODUCTION

The rhizosphere is an area surrounding the roots of plants that is most directly involved in nutrient uptake processes, typically considered to extend at least 2 - 5 mm away from the plant root [36, 37]. Within the rhizosphere, several important processes occur including changes in the nutrient distribution as a consequence of symbiotic interactions between plants and microbes [38]. The understanding of these processes is essential to the prediction and utilization of the natural nutrient cycling processes that control sustainable plant growth and development.

Understanding changes in small, inorganic nutrients including nitrate, sulfate, and phosphate in the rhizosphere has been limited by the lack of suitable techniques to reliably detect nutrients both spatially and temporally [39]. Traditionally, bulk mass spectrometry techniques have been used to examine nutrients including nitrogen, phosphorus, and carbon in the rhizosphere. Unfortunately, the use of these techniques results in a loss of the spatially resolved information necessary to determine accurate nutrient flow and distribution due to the signal averaging between different nutrients in the system [39]. Thus, to improve our understanding of spatial and temporal events associated with nutrient cycling, there is a need for new chemical visualization approaches that can accurately target and trace changes quantitatively in the availability of specific nutrient compounds.

More recently, X-ray Fluorescence Microscopy (XFM) and Nanoscale Secondary Ion Mass Spectrometry (NanoSIMS) [39] have been used to obtain spatially-resolved chemical information about nutrients *in situ* in the rhizosphere. In XFM, a focused X-ray beam is used to obtain energy resolved fluorescence spectra that identify the presence of trace elements for each position scanned. The use of XFM, especially coupled to a synchrotron source, provides sub-micron resolution, which translates into detection limits in the range sub-ppm of trace elements in the rhizosphere [40]. However, XFM is unable to detect low-Z elements such as carbon and nitrogen.

The other method that has been employed in studying rhizosphere processes, NanoSIMS, is a specific type of secondary ion mass spectrometry instrument that has been designed for high lateral resolution (down to 50 nm) imaging while still maintaining high mass resolution and high sensitivity (mg/kg range) [41]. However, it is difficult to analyze some elements because of poor secondary ion yield, the inability to quantify actual concentrations, and unobtainable chemical state information [41]. Furthermore, the field of view is limited, which means that mapping large areas is relatively slow and such experiments must be done under ultra-high vacuum, which is not conducive to biological samples [41].

Here, a new, complementary approach is introduced to address the aforementioned limitations by using Fourier transform infrared imaging (FTIRI) to image the distribution of nutrients in the rhizosphere of a woody plant. FTIRI provides an approach to simultaneously image and quantify cellular components, micro- and macronutrients, and exudates that are important to rhizosphere activity with high spatial resolution under environmentally-relevant conditions. The method is rapid and non-destructive, making it an excellent choice to reliably visualize and quantify nutrients in the rhizosphere on a sub-millimeter scale. It is particularly

well-suited for measuring inorganic ions like nitrates, phosphates and sulfates because these polyatomic macronutrients exhibit characteristic infrared vibrational frequencies that are unique.

The objective of this study was to develop an FTIRI method to study nutrient distribution in an intact plant's rhizosphere. To accomplish this, a unique experimental model system was used to minimize system complexity and to permit precise manipulation of nutrient parameters. The system was comprised of a tree species, *Populus tremuloides* (quaking aspen), and the ectomycorrhizal fungus, *Laccaria bicolor, grown in McCown Woody Plant Media (WPM).* The plant growth media is composed of WPM nutrient salts and sucrose in a Phytagel matrix, allowing the two organisms to form fully mature mycorrhizal interactions between the fungi and tree roots. [42, 43] By using FTIRI, the nitrate and sucrose distribution in the poplar rhizosphere was measured simultaneously to gain insight into nutrient sharing in mycorrhizal plant-fungus interactions. This ability to visually monitor nutrient changes with other microorganisms in the rhizosphere is a key first step towards improving our understanding of the nutrient flow processes in more complex systems.

2.3 METHODS

2.3.1 NUTRIENT MEDIA PREPARATION

McCown's Woody Plant Media (WPM), a widely used culture media for tree species, was used for each experiment [44]. The media solution was prepared by adding 2.4 g/L McCown's Woody Plant Media (WPM), 0.5 g/L 2-(*N*-morpholino) ethanesulfonic (MES), and 15 g/L mM sucrose to 1000 ml of ddH$_2$O. For each experiment requiring plant growth, two types of media were required, (1) solid media used as the rhizosphere matrix and to directly supply nutrients to the trees, and (2) liquid media used to maintain nutrient supply and hydration of the system. The

pH of the solution was then adjusted to 5.6 using a 1M KOH solution. For the solid matrix, 8 g/L of Phytagel (Sigma Aldrich Phytagel, P8169) was added, and the media was autoclaved using a pre-set liquid cycle which lasted about 70 minutes. Once the cycle was complete, the media was placed into a sterile hood (SterilGARD III, The Baker Company, Sanford, ME) utilizing aseptic technique, and the temperature was monitored using a surface sterilized thermometer placed inside the media vessel.

2.3.2 SLIDE PREPARATION (DIP-COATING)

Preparation for dipping the slides was critical. Two hot plates were surface-sterilized in the hood and calibrated to maintain a media temperature at 50°C in order to provide an ideal thickness of media (0.5 mm) during slide preparation. A sterile stir bar provided the needed media circulation to maintain a uniform temperature throughout the media.

Infrared-reflective (low-e coated) glass microscope slides were used for all infrared imaging experiments (Kevley Technologies, Chesterland, OH, USA). To provide a sterile surface on which to adhere the plant media, slides were placed in aluminum foil packets, being careful not to let the coated side of the slides come into contact with the aluminum to prevent scratching. These packets were then autoclaved on a dry / kill cycle along with all glassware, stir bars, and forceps used in the remaining procedure. After autoclaving, the slides were placed at -80˚C until use.

All dipping steps were conducted inside the sterile hood. The foil packet was removed from the freezer and placed on a bed of ice to keep the slides chilled. Slides were then dipped vertically into the freshly prepared plant media being held at 50° C, held for one second, removed and then placed horizontally on the surface of a sterile Petri plate until the WPM media solidified (~ 45 minutes) (**Figure 2-1**). The media covered roughly ¾ of the slide. Slides were

then placed vertically into 50 mL Falcon tubes containing 10 ml of liquid WPM media in preparation for subsequent steps.

2.3.3 POPLAR SEED STERILIZATION AND GROWTH

Populus tremuloides Michx seeds were obtained from the Canadian Natural Resources, National Tree Seed Center, P.O. Box 4000, Fredericton NB Canada, E3B 5P7 (http://www.atl.cfs.nrcan.gc.ca/seedcentre/seed-center-e.htm).   Seed Lot No. 9910008.0 was removed from -20°C and incubated overnight at 4°C before they were transferred to a micro-centrifuge tube and surface-sterilized using 1 ml of sterilization solution (10% commercial bleach, 250 µg/l Tween-20 and sterile water) for 5 minutes. The surface sterilization solution was removed, and the seeds were subsequently washed four times with sterile distilled water.

For germination, the poplar seeds were suspended in 0.1% sterile agarose and left for two days in the dark at room temperature. Seeds showing signs of germination were individually embedded in the gelled media near the top of each slide using a sterilized spatula and forceps. The prepared slides were then placed back into each 50 mL Falcon tube containing 10 mL of liquid media. All slides were incubated at room temperature overnight in the dark. Subsequently, the tree seedlings were transferred to a growth chamber at 22 °C, 60% humidity, and running a 16 h day/8 h night regime for 7 weeks to allow growth and development.

2.3.4 LACCARIA BICOLOR STRAIN AND CULTURE CONDITIONS

For samples incubated with *Laccaria bicolor*, free-living mycelium of the Orton strain S238N (dikaryotic) were sub-cultured and maintained on Modified Melin Norkan's (MMN) medium at 20°C in the dark. For inoculation experiments, *L. bicolor* mycelia were moved to the slides containing WPM when the *P. tremuloides* seedlings were 10 days old.   This was

accomplished by cutting the MMN media into ~ 2 mm squares under sterile conditions in the hood. These fungal "plugs" were then placed face down on each slide next to the roots of each seedling using aseptic technique. After inoculation, the seedlings were returned to the growth chamber for the reminder of the 7 weeks to allow symbiotic interactions to establish and mycorrhizal roots to form during tree development.

2.3.5 FTIRI SPECTROSCOPY AND IMAGING

Once the plants were 7 weeks old, the samples were dehydrated in an incubator at 60°C for 75 minutes and allowed to cool to room temperature. Under these conditions, the slides were observed to dry uniformly within 15 minutes; however, an additional hour of gentle drying was used to drive off any residual moisture. Slides were stored in a dark, desiccated environment until FTIRI was performed. All FTIR images were obtained from the dried samples using a Spectrum Spotlight 400 FTIR Imaging System (PerkinElmer) in transflectance mode. Spectra were collected in the mid-IR region from 4000 to 750 cm^{-1} using a 16 pixel MCT (Mercury Cadmium Telluride) array detector with a 25 µm pixel size. The spectral resolution was 8 cm^{-1} and 16 scans per spectrum were collected.

FTIR spectra were also collected from the individual components of the media, i.e. sucrose, WPM, Phytagel, and ammonium nitrate. Spectra were collected in the mid-IR region from 4000 - 750 cm^{-1} using a spectral resolution of 4 cm^{-1} and 8 scans per spectrum. Spectra of the individual components were collected using Beamline U2B at the National Synchrotron Light Source at Brookhaven National Laboratory.

2.4 RESULTS

2.4.1 POPLAR PLANT GROWTH AND DEVELOPMENT

After seed sterilization, viable *P. tremuloides* seeds began to germinate after approximately 2 days in the dark. At that time, the newly germinated seeds were transferred to prepared IR reflective slides under sterile conditions and allowed to develop at 22 °C with a 16 hour light period. After 10 days of development, lateral roots began to form[42] at which point trees requiring interaction with *Laccaria* were inoculated with small MMN media plugs containing fungal hyphae. Both the free-living seedlings and those inoculated with *Laccaria* were then allowed to develop for a total of 7 weeks. At week 3, a clear fungal hyphae network could be seen growing along the developing roots of inoculated trees. By week 5, the primary roots of the seedlings had grown to a point where they were entering the liquid WPM media at the base of each tube, and the formation of mychorrhizal lateral roots was clearly visible. At week 7, these interactions had matured, and the slides were dehydrated to remove water from the slides. Water is highly IR absorptive, and even a slight amount of water in the media limits the quality of FTIR spectra that can be obtained.

2.4.2 FTIR SPECTRA OF MEDIA COMPONENTS

The first step in characterizing the poplar rhizosphere with FTIRI was to determine the individual spectral contributions of the media to the FTIR images. The components of the plant media include Phytagel, WPM, sucrose and MES (**Table 2-1**). Phytagel, while providing a visibly clear gel, contributes a number of absorption features in the overall FTIR spectra (**Figure 2-2**). Phytagel is a high strength gelling ingredient in the growth media, consisting of a tetra-saccharide repeating unit of two glucose residues, rhamnose and glucoronic acid. Phytagel has

27

characteristic infrared vibrations that include an OH stretch (3381 cm^{-1}), asymmetric C-H stretch (2930 cm^{-1}), and asymmetric COO$^-$ stretch (1610 cm^{-1}) [45]. The Phytagel polymer absorbs strongly from 1200-950 cm^{-1} and has a number of overlapping peaks. The bands in the 905-1155 cm^{-1} region are assigned to C-O and C-C stretching modes [46] and those around 1200 -1155 cm^{-1} have contributions from the bending modes of O-C-H, C-C-H and C-O-H [46, 47]. The asymmetric carboxylate stretch at 1610 cm^{-1} does not overlap with the spectral features from other components in this system, making it the signature peak for quantifying Phytagel in these experiments.

WPM contains all of the macronutrients, micronutrients, and vitamins needed for woody plant tissue culture as described by Lloyd and McCown [44, 48]. The most noticeable infrared vibrations in the WPM spectrum occur between 1500 – 1000 cm^{-1} (**Figure 2-2**) and can be attributed to the phosphates (1092 cm^{-1}) [49], nitrates (1349 cm^{-1}) [50] and sulfates (1198 cm^{-1}) [51] found in the WPM salt mix.

Sucrose was added to the media to facilitate plant growth. Its polysaccharide structure is revealed by the broad peak at ~1000 cm^{-1} [52]. In addition, sucrose has a distinguishable infrared vibration at 925 cm^{-1} that corresponds to its glycosidic links [45, 47] which has the least overlap with other media components. Thus, the combined spectrum of the major components in the media shows that the region from 1500 - 1000 cm^{-1} has a large overlap of many spectral components, but the Phytagel and sucrose can be most easily identified through their isolated vibrations at 1610 cm^{-1} and 925 cm^{-1}, respectively [45, 52].

2.4.5 QUANTIFICATION OF NUTRIENT CONCENTRATION

In FTIR absorption spectroscopy, it is well established that absorbance is proportional to concentration as defined by the Beer-Lambert Law (A = εbc). In particular, the concentration of

nitrate in the poplar rhizosphere was determined using the Beer-Lambert Law ($A = \varepsilon bc$), where A is the FTIR absorbance at a particular wavelength, ε is the absorption coefficient at a particular wavelength, b is the sample thickness, and c is the sample concentration. However, as is noted in the Beer-Lambert Law, knowledge of the absorption coefficient and sample thickness must be known in order to determine the nutrient concentration. To calculate the Phytagel thickness, the fringing effect of thin films was applied (see Supplemental Information). The average Phytagel thickness using this method was found to be 2.4 ± 0.07 μm. The error of the technique was determined based on the 3% error obtained from a control polyimide film.

The absorption coefficient was calculated for the asymmetric carboxylate peak at 1610 cm^{-1} because it has very little overlap with the spectra of the micro/macro nutrients or plant components. By using the calculated Phytagel thickness of 2.4 μm, a Phytagel concentration of 0.008 mM, and a measured absorbance of 0.3 for the asymmetric carboxylate peak at 1610 cm^{-1}, the Beer-Lambert Law showed that the extinction coefficient for Phytagel at 1610 cm^{-1} to be 1.56×10^5 cm^{-1} mM^{-1}.

2.4.5.1 NITROGEN DETECTION

Assignment of nitrate spectral features: In order to quantify the nutrients in the rhizosphere, nitrogen in this case, the spectral contributions of ammonium ($NH4^+$) and nitrate ($NO3^-$) were first identified. The FTIR spectrum of $^{14}NH_4^{14}NO_3$ can be seen in **Figure 2-3,** where two strong bands were observed at 1340 and 1432 cm^{-1}. In order to assign these peaks, isotopically-substituted NH_4NO_3 was examined. From the FTIR spectrum of $^{14}NH_4^{15}NO_3$, it can be seen that the 1340 cm^{-1} band shifts to 1305 cm^{-1} due to the larger reduced mass of the heavier $^{15}NO_3$ isotope, indicating that this peak is assigned to the NO_3 stretching vibration. Also, the $^{14}NO_3$ bending vibration was observed at 827 cm^{-1}, which shifted to 806 cm^{-1} upon $^{15}NO_3$

substitution, confirming the assignment (**Figure 2-3 inset**). A similar analysis for the $^{14}NH_4$ bending vibration mode, which was found at 1432 cm^{-1}, was shown to shift to 1425 cm^{-1} for $^{15}NH_4$.

2.4.5.2 CALIBRATION CURVE

Once the spectral features of nitrate were determined, quantification of the nitrate content in the rhizosphere was done using a calibration curve of nitrate absorbance intensity versus nitrate concentration. To generate the calibration curve, infrared-reflective slides were dip-coated in Phytagel media that contained 7, 10, 15 or 20 mM ammonium nitrate and allowed to dry. For each slide, twenty FTIR spectra were collected in transflectance mode at different locations on the slide. The slide preparation process was repeated three times. An average spectrum was calculated for each ammonium nitrate concentration from the 60 spectra. Each average spectrum was then baseline-corrected using points at 3900, 1800, 1510, 1210, and 790 cm^{-1}. The four baselined spectra were normalized such that the Phytagel carboxylate peak at 1610 cm^{-1} had an absorbance value of 0.2 (**Figure 2-4A**). The absorbance intensity at the nitrate stretching vibration (1340 cm^{-1}) was then plotted against the nitrate concentration to yield the calibration curve in **Figure 2-4B**.

2.4.5.3 NUTRIENT UNIFORMITY IN THE ABSENCE OF PLANT TISSUE

To confirm a uniform nutrient distribution on the Phytagel slide in the absence of a plant, FTIR images were collected from the control slides described above. Specifically, FTIR maps measuring 1 mm^2 (40x40 pixels) were collected at five different regions on each slide. An integration profile of the nitrate peak was generated by calculating the peak height at 1340 cm^{-1} using a linear baseline from 1505 - 1255 cm^{-1}. Similarly, an integration profile of the Phytagel

peak was generated by calculating the peak height at 1610 cm^{-1} using a linear baseline from 1775 - 1545 cm^{-1}. In order to account for Phytagel thickness variations in the sample, a normalization matrix was generated that yielded a constant Phytagel intensity of 0.2 at each pixel. Then the nitrate image was normalized to thickness by applying the normalization matrix. Finally, the nitrate concentration was calculated from the normalized nitrate image using the calibration curve from **Figure 2-4B**. An average percent difference of 4% was calculated across 20 maps. Thus, for a standard Phytagel slide made with 7 mM nitrate, the nitrate concentration varied from 7.0 ± 0.28 mM, which is negligible compared to the plant's influence on the media.

2.4.5.4 NUTRIENT DISTRIBUTION IN THE PRESENCE OF PLANT TISSUE

The visible and infrared images of a seven week old Poplar plant lateral root grown with *Laccaria* is shown in **Figure 2-5**. The visible image clearly shows the root colonization by the fungi. *L. bicolor* is an ectomycorrhizal fungus that forms a dense hyphal covering (fungal sheath or mantel) over the root from which hyphae grow into the intercellular spaces forming a net of internal hyphae (i.e. the Hartig net) around the root cortex cells, but do not penetrate the cell walls [27], [37]. This hyphal sheath forms an extension of the plant roots to increase the surface area of soil explored [37] called the extra-radical mycelium (ERM). The fungal biomass can be seen as brown clusters around the plant root is highlighted in **Figure 2-5A**. The infrared image, **Figure 2-5B,** shows that a nitrate gradient exists, where reduced amounts of nitrate are seen further from the plant root and its primary fungal biomass.

To obtain a quantitative assessment of this nitrate gradient, the calibration curve in **Figure 2-4B** was used to calculate the nitrate concentration at each pixel. The line plot in **Figure 2-5D** shows how the nitrate concentration changes moving away from the plant root. **Figure 2-5D** shows that the nitrate concentration is at its lowest, 0 to 3 mM, within 1000 microns from the

plant root, increases up to 35 mM at 1500 microns and decreases almost steadily from 17 mM at 3000 microns to 7 mM at 5500 microns. This low concentration of 0 – 3 mM nitrate within the first 1000 microns is likely due to the plant's uptake and consumption of the nitrate. The increased nitrate supply that surrounds this depleted region may be due to sequestration of nitrate by the fungi from the broader rhizosphere, hence a decrease in nitrate concentration exists following this available nutrient pool to the wider rhizosphere. Such pooling of high nitrate concentrations close to the root is in line with many other reports that indicate N sources are transferred from the fungi to the plant in exchange for carbon rich metabolites, such as simple hexoses derived from plant photosynthesis [53-55].The phenomenon is well characterized, but this is first report to visually characterize such activity at the chemical level.

In addition to nitrate, the sucrose concentration in the rhizosphere (**Figure 2-5C**) was also analyzed. Interestingly, **Figure 2-5D** shows that the sucrose concentration is low near the root, 3-6 mM within the first 1000 microns and increases further away from the root until it reaches to the concentration of the control media, 40 mM, at around 5500 microns. This pattern suggests that the sucrose, which is the carbon source in the media, is consumed by the fungi, hence the decrease in sucrose concentration in areas where the fungi is present.
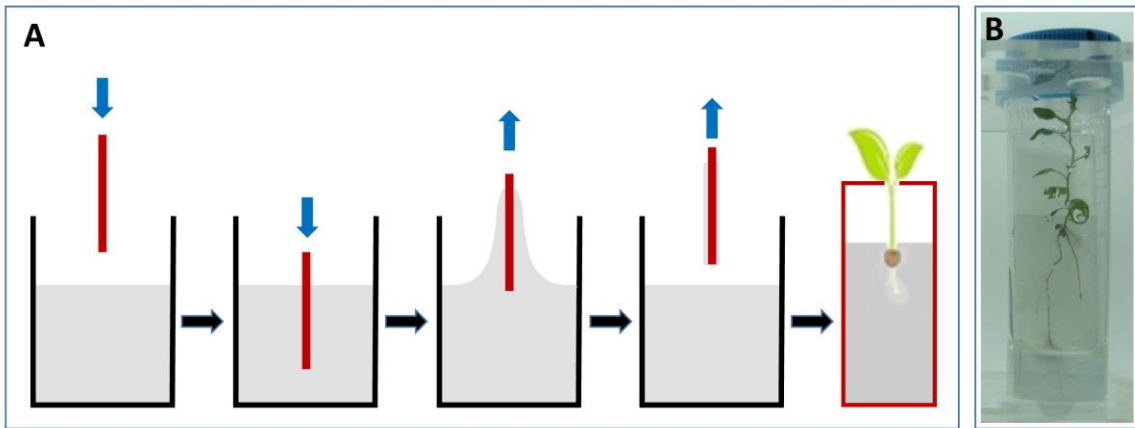
Figure 2-1. (A) Slide preparation for growing *Populus tremuloides*. A sterile chilled reflective glass slide was immersed into a 50° C WPM + Phytagel solution. As the slide is pulled from the solution, a layer of media deposits over the slide which becomes a thin gel (~0.5 mm) as the Phytagel solidifies. A poplar seedling is then embedded into the gelled media at the top end of the slide and is allowed to grow for 5-7 weeks either with or without fungal interaction. **(B)** *Populus tremuloides* grown on an IR-reflective glass slide in a conical tube. The image shows how the plant roots grow vertically downwards on the slide. The seedlings receive nutrients from the Woody Plant Medium (WPM) which facilitates the plant growth and interaction with *Laccaria.*
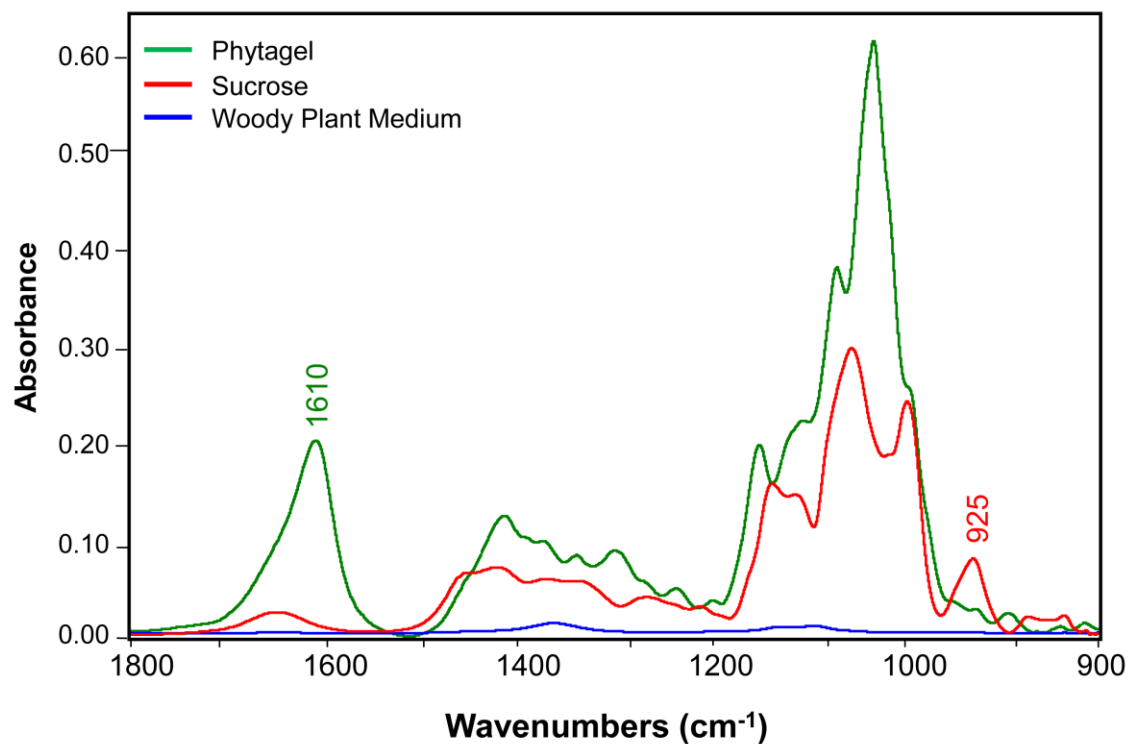
Figure 2-2 FTIR spectra of the components in the plant media: Phytagel (green), Woody Plant Medium (WPM) (blue) and sucrose (red). In the Phytagel spectrum, the carboxylate ester peak at 1610 cm^{-1} and polysaccharide peaks (1000 – 1200 cm^{-1}) are most prominent. The glycosidic bond in sucrose is present at 925 cm^{-1}. Primary nutrients (nitrates, phosphates, sulfates) are found in WPM and have vibrational modes between 1300 –1500 cm^{-1}. WPM has a negligible contribution compared to other components in the media.
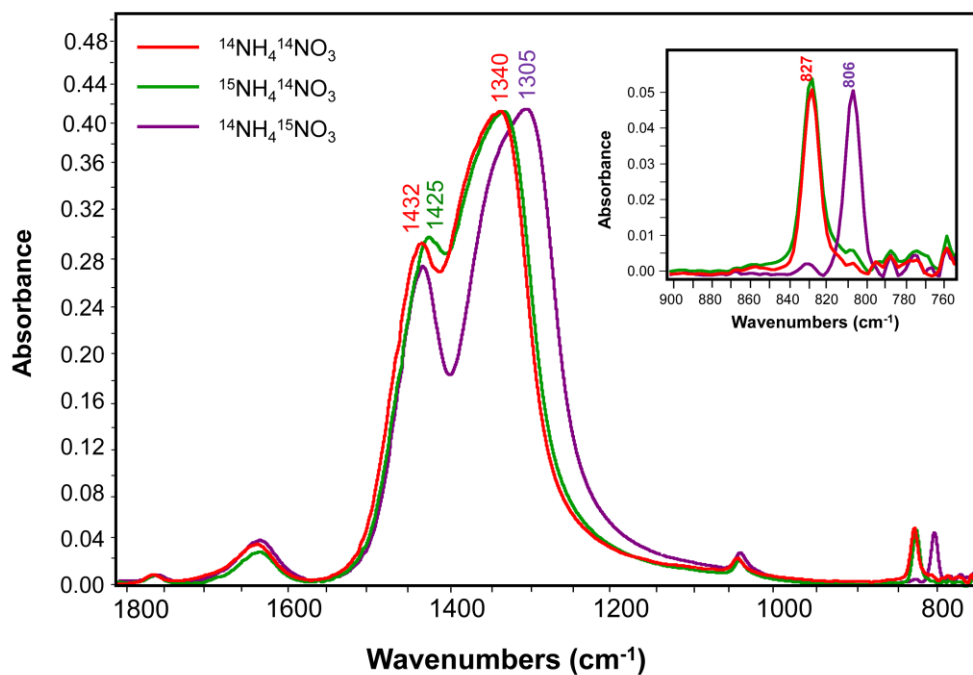
Figure 2-3. FTIR absorption spectra of $^{14}NH_4{}^{14}NO_3$, $^{14}NH_4{}^{15}NO_3$, and $^{15}NH_4{}^{14}NO_3$ showing the $^{14}NH_4{}^+$ bending vibration at 1432 cm^{-1} and $^{14}NO_3{}^-$ stretching vibration mode at 1340 cm^{-1}. The inset shows the $^{14}NO_3{}^-$ bending mode at 827 cm^{-1}. Upon isotopic substitution, the $^{15}NH_4{}^+$ bending vibration shifts to 1425 cm^{-1}. The $^{15}NO_3{}^-$ stretching vibration and the $^{15}NO_3$ bending vibration shift to 1305 and 806 cm^{-1}, respectively.
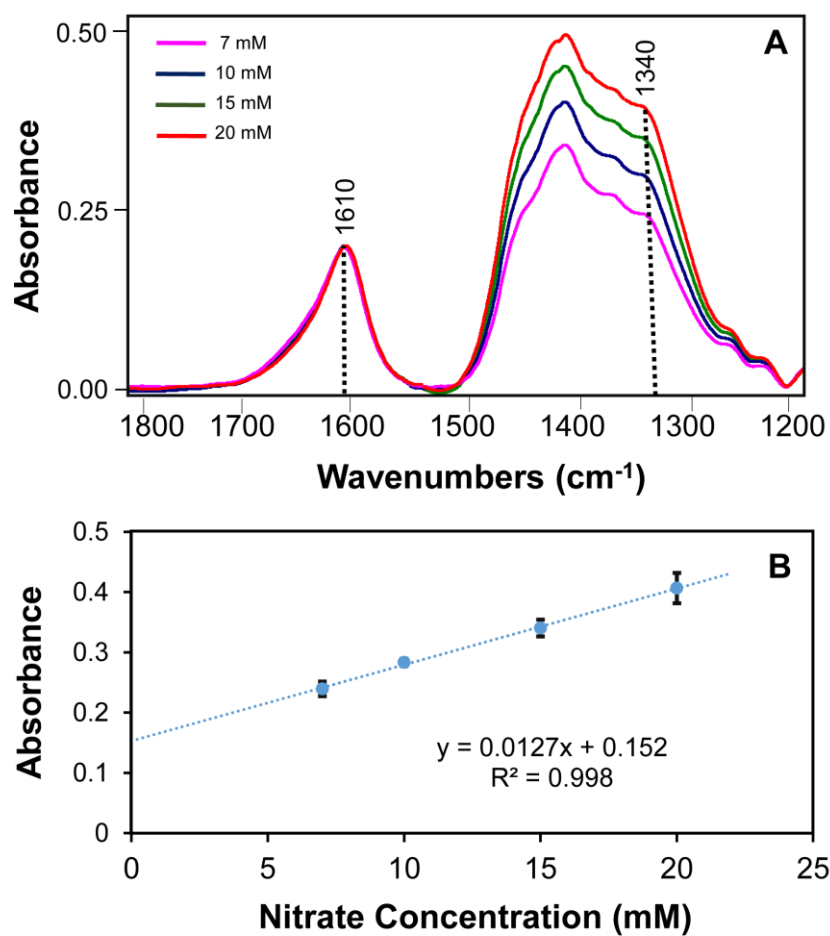
Figure 2.4 **(A)** FTIR absorption spectra of the Phytagel media with increasing concentrations of ammonium nitrate at 7, 10, 15, and 20 mM. **(B)** Calibration curve of nitrate absorbance at 1340 cm^{-1} *vs.* nitrate concentration. The line plot shows a direct linear correlation between nitrate absorbance and concentration.
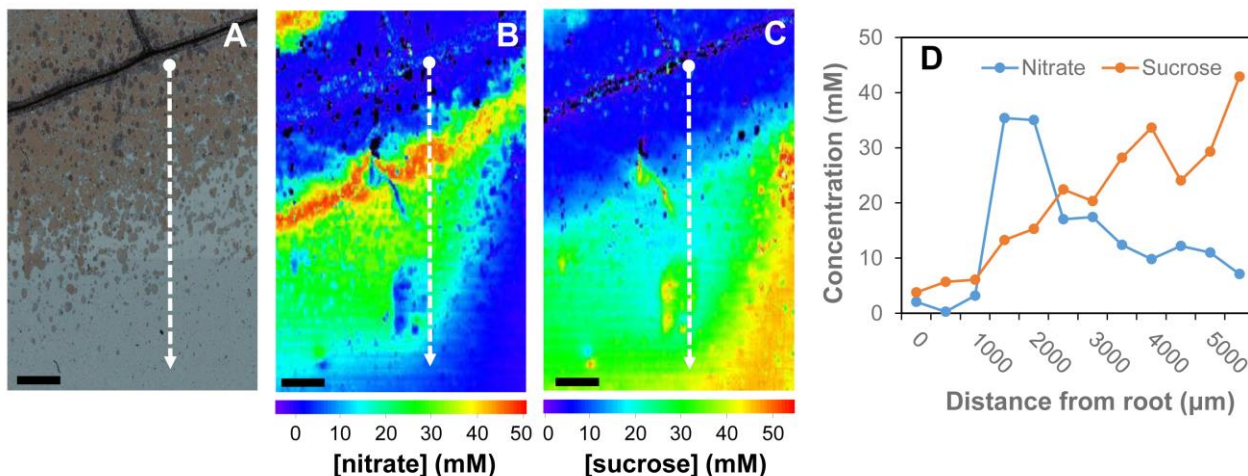
Figure 2-5 (A) Visible image of a Poplar plant root embedded in Phytagel media. Brown regions represent fungal biomass. The image shows fungal colonization over the plant root. **(B)** FTIR image of the same sample showing the distribution of nitrate in the rhizosphere. The image shows that the nitrate concentration is elevated in the regions of high fungal colonization and decreases away from the plant root as the fungal population decreases. **(C)** FTIR image showing distribution of sucrose in the rhizosphere. The plot shows that the sucrose concentration increases away from the plant root as the fungal population decreases. **(D)** Plot of nitrate and sucrose concentration versus distance from the poplar plant root. Points on the plot were extracted from the line profiles in Figures **2-5B** and **2-5C** for nitrate and sucrose, respectively. The trend suggests that there is symbiotic sharing of nutrients between the plant and the fungi where the fungi consumes the sucrose and sequesters nitrate for the plant's use. Scale bar is 1 mm for all images.

2.5 DISCUSSION AND CONCLUSIONS

Healthy soil is an important resource in both natural and agricultural ecosystems. It harbors both chemical and biological sources of nutrients that are required for plant growth, reproduction, insect and pathogen resistance, and response to changing environments. However, current agricultural practices rely heavily on the meticulous management of chemical nutrients. In natural ecosystems, nutrients in the rhizosphere are taken up by microorganisms like fungi and bacteria and are delivered to plants during interactions with plant roots in exchange for fixed carbon [56, 57]. While such symbiotic relationships play an essential role in the regulation of soil nutrient cycling and subsequent carbon management, the complexity and variation of such natural systems has hindered the accurate assessment of the factors that maintain these important nutrient cycling interactions. This study is the first of its kind to visualize and quantify the nutrient availability and spatial location of key nutrient sources during such symbiotic associations. It thus represents a key step toward enhancing our understanding of the biological nutrient cycling pathways that are so essential to the development of both above- and below-ground biomass.

Nitrogen is an essential macronutrient required for plant growth and reproduction,[25] and its availability directly limits net primary productivity [27, 58, 59]. Because plants in natural systems have a limited ability to utilize organic forms of nitrogen, the supply of nitrogen derived from the activity of the soil life is essential to biomass production. Nitrate is the primary form of nitrogen available to plants [60]. By using FTIRI, the nitrate distribution in the poplar rhizosphere was mapped. The chemical images obtained from the rhizosphere provided both visual and quantitative evidence for the symbiotic sharing of nutrients between the plant and an ectomycorrhizal fungus, where the nitrate concentration was 5-fold higher around the fungal/root

mantel, suggesting sequestration of nitrate from the media toward the plant root. The highest nitrate concentration was 35 mM around 1500 microns away from the plant root, which then decreased to 7 mM at 5500 microns, which is the baseline concentration in the media. Similarly, the sucrose used in the growth media as a carbon source was depleted to 3-6 mM around the mycorrhizal roots, suggesting its consumption by the fungus. It steadily increased to ~ 40 mM at 5500 microns away from the plant root. However, it should be noted that *Laccaria* does not possess the invertase enzyme that breaks sucrose into glucose and fructose. Therefore, it is likely that invertase is secreted from the plant roots into the media, thus facilitating breakdown of sucrose with subsequent uptake of glucose and fructose [61].

Other studies have shown that carbon availability from the host triggers fungal nitrogen uptake and transport to plants during mychorrizal symbiosis.[53-55, 62] For example, Fellbaum et al. showed that an increase in carbon availability via the addition of 25 mM sucrose to the root compartment increased the uptake of inorganic and organic nitrogen sources by the extra-radical mycelium (ERM) and transport to the root which resulted in two times as much nitrogen in the root tissue [62]. This increase in nitrogen is facilitated by changes in fungal gene expression, including increases in the abundance of transcripts associated with nitrate transport[53, 54]. Studies also indicate that high affinity N transporters of fungi are highly expressed in the ERM but down regulated in the IRM which favors active absorption of nutrients like NO_3^- in the ERM, which plays a role in developing a strong concentration gradient across the mycorrhizal interface [53]. This is consistent with the data presented here, which clearly demonstrates a nitrate gradient being formed surrounding the poplar - *Laccaria* mycorrhizal roots in the ERM. While significant progress has been made in understanding the N transport pathways of mycorrhizal fungi, it is still currently unknown in what form the nitrogen is transported from the fungal

hyphae into the mycorrhizal Hartig net within the plant root cortex cells. Furthermore, the transport of other nutrients involved in such symbiotic interactions is not clear, and it is unknown how other nutrients except phosphorus, contribute to the carbon costs of symbiosis for the host plant [55].

In this work, it was shown that FTIRI can reliably detect and quantify the nitrate and sucrose distribution *in situ* in the rhizosphere of poplar, which, with developing model systems, can help provide an understanding of the cost (carbon) to benefit (nutrient gain) ratio of symbiotic associations. The results showed evidence for symbiotic transport and sharing of nutrients between the plant and the ectomycorrhizal fungi, where the nitrate concentration was high around the root-associated fungi, suggesting sequestration from the media toward the plant root. Similarly, the sucrose used in the growth media as a carbon source was depleted around the fungi, suggesting its uptake and consumption.

In the future, this approach can be extended further to detect other essential inorganic nutrients including phosphates and sulfates. Its application is also suitable for studying other plant species or broader plant-microbe ecosystems that combine various plants, fungi, and bacteria while still having control of the system variables. Moreover, aided synchrotron infrared beams, subcellular analysis of the interface between the plant's root hairs and the rhizosphere can be pursued. The high brightness of a synchrotron source improves the spatial resolution to the diffraction limit of 2 – 10 µm and improves spectral quality compared to a conventional globar source. In addition, it is possible to collect data more quickly and to oversample, which can improve the spatial resolution even further through deconvolution [63]. By analyzing the plant's root hairs in the presence and absence of ectomycorrhizal fungi, a better understanding of the fungi's role in nutrient uptake in this symbiotic union will be possible. This ability to monitor

nutrient changes with other microorganisms in the rhizosphere is a key step for understanding environmental nutrient flow processes.

With FTIRI providing a mechanism to probe how nature so effectively controls the availability of soil nutrients through the activity of beneficial microorganisms, future improvements may be made to land management programs that will allow more sustainable plant growth on an industrial scale by taking advantage of already existing plant-microbe relationships.

2.6 SUPPLEMENTAL INFORMATION

This supplemental information presents additional information on the components of McCown Woody Plant medium and the methods used to determine the thickness of phytagel deposited on each slide.

2.6.1 DETERMINATION OF THE PHYTAGEL THICKNESS USING THE FRINGING EFFECT

The concentration of nitrate in the poplar rhizosphere was determined using the Beer-Lambert Law ($A = \varepsilon bc$), where A is the FTIR absorbance at a particular wavelength, ε is the absorption coefficient at a particular wavelength, b is the sample thickness, and c is the sample concentration. However, as is noted in the Beer-Lambert Law, knowledge of the absorption coefficient and sample thickness must be known in order to determine the nutrient concentration. To calculate the Phytagel thickness, the fringing effect of thin films was applied. To do so, the Phytagel matrix was dried down to reduce sample thickness and to remove the strong, broad absorption bands of water that would contribute to the spectra. The dried Phytagel film was placed into a FTIR sandwich cell with a 13 mm^2 round opening and five FTIR spectra were

collected from different regions in transmission mode from 7000 - 750 cm^{-1}, using a spectral resolution of 4 cm^{-1} and 128 scans per spectrum. A similar procedure was followed for a 8 μm-thick Kapton (polyimide) film as a control. To calculate the Phytagel thickness, the fringing effect of thin films was applied using the following equation:

$$b = N \,/\, 2n \,(\upsilon_1 - \upsilon_2)$$

where b = path length of the cell, n = the refractive index of the material, N = the number of fringes within a given spectral region, and υ_1 and υ_2 are the start and end points of that spectral region.

The fringing effect from the Kapton polyimide film, used as a reference to determine the accuracy of this method, revealed 3 fringes in the spectral region from 6660 - 5560 cm^{-1} (**Figure 2-6**). Using its refractive index of 1.7, the calculated thickness was 8.2 ± 0.2 μm, which was very close to the manufacturer's reported thickness of 8 μm. For the Phytagel film, 2 fringes were observed in the spectral region from 7075 - 4345 cm^{-1}. We estimated a refractive index of 1.5 for Phytagel based on the refractive index of other polymers in its class such as poly vinyl alcohol, which resulted in a calculated thickness of 2.4 ± 0.07 μm. The error of the technique was determined based on the 3% error obtained from the polyimide film.

$$N = 2$$

$$v_1 \qquad T = \frac{N}{2n(v_1 - v_2)} \qquad v_2$$
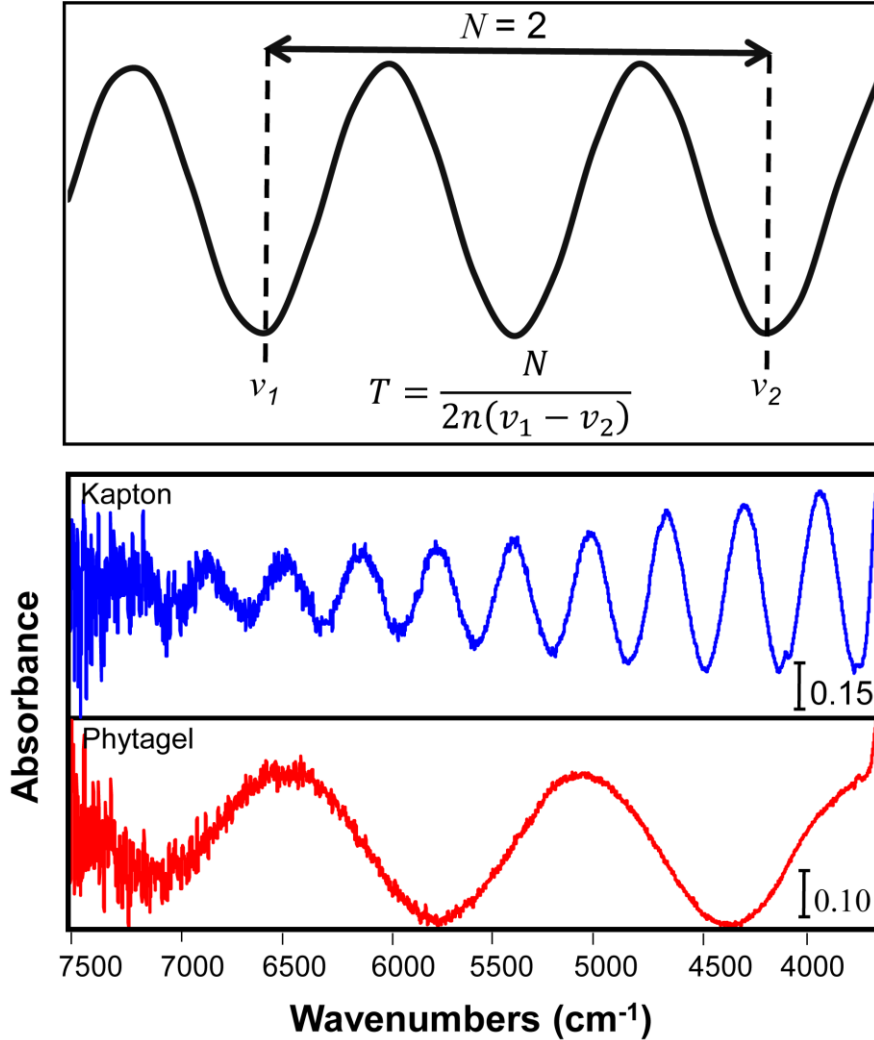
Figure **2-6** Interference fringes in the FTIR transmission spectra of free standing films of Kapton polyimide (blue) and Phytagel (red). The fringing effect was used to calculate the thickness of the dried Phytagel film, which was found to be 2.4 µm. An example of a Kapton polyimide reference film is also shown. The refractive index used in calculating the film thickness was 1.7 and 1.5 for polyimide and Phytagel respectively.

Table 2-1. Composition of nutrient medium used for growing plants

Component	Concentration (mM)
Phytagel	0.008
Sucrose	40
MES (2-ethanesulfonic acid)	2.6

Woody Plant Medium

Ammonium nitrate	5.0
Potassium sulfate	5.0
Magnesium sulfate	2.0
Calcium nitrate	2.0
Potassium Phosphate	1.0
Calcium chloride	0.6
Copper Sulfate	0.001
EDTA	0.1
Boric acid	0.1
Magnesium sulfate	0.1
Molybdic acid	0.002
Ferrous sulfate	0.1
Zinc sulfate	0.03
Myo-Inositol	0.5
Glycine	0.03
Thiamine HCl	0.006
Nicotinic Acid	0.005
Pyridoxine HCl	0.002

CHAPTER 3

EXAMINATION OF THE EFFECTS OF MYCORRHIZAL FUNGI ON NITROGEN AVAILABILITY IN THE POPLAR RHIZOSPHERE

3.1 ABSTRACT

Nitrogen is one of the most important elements for biomass production. Its uptake is dependent upon the external N availability and a plant's need. Growth promoting organisms like mycorrhizal fungi improve the nutrients available to plants, which causes changes in the distribution of external N levels. In this study, Fourier Transform Infrared Imagine (FTIR-I) was used to examine the distribution of N in the rhizosphere of Poplar seedlings grown in the presence of the mycorrhizal fungus, *Laccaria bicolor*. The FTIR spectral region from 1550–1200 cm^{-1}, containing characteristic bands for nitrate and ammonium, was examined using partial least squares regression (PLSR). A set of reference FTIR spectra from varying concentrations of ammonium and nitrate solutions were prepared and PLS calibration models for nitrate and ammonium were developed. The models were tested using the root-mean-square errors of cross-validation for nitrate and ammonium concentrations, which were 2.84% and 3.11% respectively. It was shown that NH_4 is the preferred source of N for consumption in both high N and low N conditions and NO_3 is assimilated rather than consumed in plants grown with mycorrhizal fungi. Furthermore, the *Laccaria bicolor* was able to assimilate approximately six times more nitrate than the plant only system grown in the control N concentration. By using FTIR-I, it is possible to image nutrients in situ in the rhizosphere of plants, which is important for understanding the molecular dynamics that enhances biomass production, especially when grown with mycorrhizal fungi.

3.2 INTRODUCTION

Nitrogen is the most important nutrient for plant growth and development. It is needed to synthesize compounds including proteins, lipids and carbohydrates that facilitate the production of biomass. This nitrogen is primarily acquired from ammonium and nitrate in the soil[64]. Although organic sources of nitrogen can be utilized by plants, many of these sources must first be broken down into amino acids and simple peptides by microorganisms [65]. To utilize the N available in the soil, plants need to first sense the N molecules and then transport them to various plant cells upon demand. The transport of N from the soil is determined by the availability of external N, internal N concentration, and the plant's need for the nutrient. Under low N conditions, the need for nitrogen becomes even more important to support plant growth. Plant growth promoting organisms include mycorrhizal fungi and nitrogen fixing bacteria, which provide additional avenues for plants to obtain useable nitrogen. Mycorrhizal fungi are able to scavenge the soil in zones far broader than the plant itself, exploiting untapped nutrient sources by growing extensively and broadly into the soil. The small diameter of fungal hyphae, ~5 μm, also means that fungi can efficiently absorb and shuttle nutrients back to the host plant. Similarly, growth promoting bacteria are able to break down organic sources of nitrogen into amino acids or simple peptides and convert nitrogen gas into inorganic ions [66]. Monitoring how the spatial and temporal concentrations of N and its chemical form changes in the rhizosphere is important for understanding the effect of N availability on triggering systemic signals, plant nutrition and development.

Traditionally, bulk methods have been utilized to measure N concentrations in the soil, which provides an average measure of soil nutrients. Here, by using FTIR-I, it was possible to obtain chemical snapshots of the nutrient distribution in the rhizosphere 'in situ', including

inorganic N sources such as nitrate anfigd ammonium. Because there is considerable overlap in the nitrate and ammonium IR vibrational bands with other components in the plant media, it was necessary to utilize multivariate analysis to determine the concentration of nitrate and ammonium ions in the samples. Specifically, calibration solutions were prepared and measured using FTIR-spectroscopy, followed by spectral modeling using a partial least squares regression algorithm, which was used to evaluate the concentrations of nitrate and ammonium in the rhizosphere of Poplar seedlings grown under different conditions.

3.3 MATERIALS AND METHODS

3.3.1 NUTRIENT MEDIA PREPARATION

The experiment required media containing two concentrations of nitrogen: control media (14 mM N), and low nitrogen media (3.5 mM N). Stock solutions for macro- and micro-nutrients and vitamins were prepared in the concentrations presented in the media component (Table 3-1). To avoid any variation in the preparation of the media, a single 2000 ml batch of media was first prepared with all non-nitrogen containing stock solutions including the vitamins. This batch was then split in half and the correct amounts of nitrogen were added from the containing stock solutions (NH_4NO_3 and $Ca(NO_3)_2 \cdot 2H_2O$).

For each 1000 ml of control and low nitrogen media, 600 ml of each batch was kept in the liquid form and 400 ml was converted to solid media by adding 3.2 g of phytagel (8 g/L). The media was supplemented with 1.5% sucrose (30 ml/L of sterile 50% sucrose solution) as a carbon source after autoclaving.

3.3.2 SLIDE PREPARATION (DIP-COATING):

Preparation for dipping the slides was critical. Two hot plates were surface-sterilized in the hood and calibrated to maintain a media temperature at 50°C in order to provide an ideal thickness of media (0.5 mm) during slide preparation. A sterile stir bar provided the needed media circulation to maintain a uniform temperature throughout the media.

Infrared-transparent calcium fluoride slides were used for all infrared imaging experiments. To provide a sterile surface on which to adhere the plant media, slides were placed in aluminum foil packets, being careful not to let the slides come into contact with the aluminum to prevent scratching. These packets were then autoclaved on a dry / kill cycle along with all glassware, stir bars, and forceps used in the remaining procedure. After autoclaving, the slides were placed at -80°C until use.

All dipping steps were conducted inside the sterile hood. The foil packet was removed from the freezer and placed on a bed of ice to keep the slides chilled. Slides were then dipped vertically into the freshly prepared plant media being held at 50° C, held for one second, removed and then placed horizontally on the surface of a sterile Petri plate until the WPM media solidified (~ 45 minutes) (**Figure 2-1**). The back of the slides were then wiped with a sterilized clean cloth. The media covered roughly ¾ of the slide. Slides were then placed vertically into 50 mL Falcon tubes containing 10 mL of liquid WPM media in preparation for subsequent steps.

3.3.3 PLANT GROWTH

To examine the effect of symbionts on N distribution in the Poplar rhizosphere, four different growth conditions were examined: (1) plant-only, (2) plant + bacteria, (3) plant + fungus, and (4) plant, fungus + bacteria.

3.3.3.1 POPLAR SEED STERILIZATION AND GROWTH

Populus tremuloides Michx seeds were obtained from the Canadian Natural Resources, National Tree Seed Center, P.O. Box 4000, Fredericton NB Canada, E3B 5P7 (http://www.atl.cfs.nrcan.gc.ca/seedcentre/seed-center-e.htm). Seed Lot No. 9910008.0 was removed from -20°C and incubated overnight at 4°C before they were transferred to a micro-centrifuge tube and surface-sterilized using 1 ml of sterilization solution (10% commercial bleach, 250 µg/l Tween-20 and sterile water) for 5 minutes. The surface sterilization solution was removed, and the seeds were subsequently washed four times with sterile distilled water.

For germination, the poplar seeds were suspended in 0.1% sterile agarose and left for two days in the dark at room temperature. Seeds showing signs of germination were individually embedded in the gelled media near the top of each slide using a sterilized spatula and forceps. The prepared slides were then placed back into each 50 mL Falcon tube containing 10 mL of liquid media. All slides were incubated at room temperature overnight in the dark. Subsequently, the tree seedlings were transferred to a growth chamber at 22 °C, 60% humidity, and running a 16 h day/8 h night regime for seven weeks to allow growth and development.

3.3.3.2 *LACCARIA BICOLOR* STRAIN AND CULTURE CONDITIONS

For samples incubated with *Laccaria bicolor*, free-living mycelium of the Orton strain S238N (dikaryotic) were sub-cultured and maintained on Modified Melin Norkan's (MMN) medium at 20°C in the dark. For inoculation experiments, *L. bicolor* mycelia were moved to the slides containing WPM when the *P. tremuloides* seedlings were 10 days old. This was accomplished by cutting the MMN media into ~ 2 mm squares under sterile conditions in the hood. These fungal "plugs" were then placed face down on each slide next to the roots of each seedling using aseptic techniques. After inoculation, the seedlings were returned to the growth chamber for the remainder of the seven weeks to allow symbiotic interactions to establish and mycorrhizal roots to form during tree development.

3.3.3.3 INOCULATION OF POPULUS TREMULOIDES WITH PSEUDOMONAS FLUORESCENS

For plant samples incubated with *P. fluorescens* strain PF-01, a toothpick inoculation of the bacteria was done into 2 mL of WPM liquid media for 16 hours at 20 C in a shaker at 220 RPM. Two days after the Poplar seedlings were transplanted onto the calcium fluoride slides, a 50µl volume of bacteria was dripped onto the media next to root of *P. tremuloides*. After inoculation, the seedlings were returned to the growth chamber for the remainder of the seven weeks to allow symbiotic interactions to establish and mycorrhizal roots to form during tree development.

3.3.3.4 INOCULATION OF POPULUS TREMULOIDES WITH LACCARIA BICOLOR AND PSEUDOMONAS FLUORESCENS

Two days after the seedlings were transplanted onto the slides, they were inoculated with fungus and bacteria. Two mm square slices (making sure to include the fungal hyphae) were cut and transplanted onto slides close to the *P. tremuloides* root growth. A toothpick inoculation of the bacteria *Pseudomonas fluorescens* PF-01 was done into 2 mL of WPM liquid media for 16 hours at 20 C in a shaker at 220 RPM. A 50 µl volume of the bacteria was dripped onto the media next to root of *P. tremuloides*. After inoculation, the seedlings were returned to the growth chamber for the remainder of the seven weeks to allow symbiotic interactions to establish and mycorrhizal roots to form during tree development.

3.3.4 CALIBRATION STANDARDS

The calibration standards were prepared with the non-nitrogen containing nutrients and vitamins stock solution. For the nitrate calibration model, eight solutions were all made with 6 mM ammonium chloride. These eight solutions contained 0, 1, 3, 5, 9, 15, 25 and 40 mM nitrate in 20 mL of non-nitrogen containing media. For the ammonium calibration model, six solutions were made with a constant concentration of 9 mM nitrate and 0, 1, 3, 6, 12, 20 mM ammonium in 20 mL of non-nitrogen containing media. In each solution, 8 g/L of Phytagel was added. The media was supplemented with 1.5% sucrose after autoclaving. Slide preparation and dipping was done as described above.

3.3.5 FTIRI SPECTROSCOPY AND IMAGING

All FTIR spectra and images were acquired using a Spectrum Spotlight 400 FTIR Imaging System (PerkinElmer) in transmission mode. Infrared images were collected in the mid-IR region from 4000 to 750 cm^{-1} using a 16 pixel MCT (Mercury Cadmium Telluride) array detector with a 25 µm pixel size. The spectral resolution was 8 cm^{-1} and 16 scans per spectrum were collected. FTIR spectra from calibration standards were collected in the mid-IR region from 4000 - 750 cm^{-1} using a spectral resolution of 4 cm^{-1} and 8 scans per spectrum.

3.3.6 PARTIAL LEAST SQUARES (PLS) REGRESSION

Partial Least Squares (PLS) regression is a statistical technique that is used to build predictive models of multivariate data. The PLS algorithm finds the factors that best describe the variations in the predictors (infrared spectra) and responses (concentration of N ions). The PLS models were developed using Opus Quant2 software. The spectral range of interest, from 1550 to 1200 cm^{-1}, was chosen because it contained the strongest contributions from the nitrate and ammonium vibrational peaks [67]. In total, 171 data points were employed in building the models. The spectra were vector normalized as part of the pre-processing treatment to reduce any absorbance intensity bias due to differences in sample thickness. Leave-one-out cross validation modeling method was employed. For this process, seven out of the eight samples were used as the training dataset for the calibration set to test the one sample left out for the nitrate model. This iteration was done so that all unique samples were left out once and tested. This process was done for the ammonium model as well. The models were evaluated using the root mean square error of cross validation (RMSECV), coefficient of determination (R^2), and ratio of performance

to deviation (RPD). Spectra from the infrared maps were used to calculate the ammonium and nitrate concentrations.

3.4 RESULTS

Figure 3-1 shows a plant grown with (**Figure 3-1D**) and without fungus (**Figure 3-1A**). The plant grown with the fungus in **Figure 3-1D** grew broader leaves in a larger quantity than the plant which grew without the fungus in **Figure 3-1A**. The infrared correlation images in **Figure 3-1C** and **3-1F** were generated by measuring similarities between a spectrum from *L. bicolor* (**Figure 3-1G***)* and each spectrum at every pixel in the infrared image. The root in **Figure 3-1B** and root tip in **Figure 3-1E** correlate to infrared images in **Figure 3-1C** and **3-1F** respectively. From the image, we see that the fungus is highly dense (pink colored region) around the plant's root in the plant+ fungus image while the plant only image shows that there is no fungus present in the rhizosphere.

The most distinguishing infrared spectral signatures from the growth matrix are due primarily to Phytagel, WPM and sucrose. The standard spectra in **Figure 3-2A** show that nitrate has infrared stretching vibrations at 1416 and 1334 cm^{-1}, and a bending vibration at 820 cm^{-1} while ammonium has bending vibrations at 1444 and 1404 cm^{-1} and stretching vibrations at 3140, 3049 and 2810 cm^{-1}. The combined WPM, sucrose and Phytagel spectrum shows that there are several other peaks in the 1500 to 1250 cm^{-1} region from these sources. The second derivative spectra in **Figure 3-2B** highlights the shoulder in the nitrate absorption band at 1465 cm^{-1}.

The validation plots from the two models constructed show fitted vs true concentration of nitrate and ammonium and produced a linear fit with coefficient of determination (R^2) values of 96% and 80.4% respectively (**Figure 3-3A and Figure 3-3B**). Three and two PLS components

were deemed significant to model the nitrate and ammonium spectra (**Figure 3-3C**). The other statistics measured for the two models made included the error terms, root mean square error of cross validation (RMSECV) and root mean square error of estimation (RMSEE), and the ratio of performance to deviation (RPD). The nitrate model measured: RMSECV: 2.84, RMSEE: 2 and RPD: 4.81. The ammonium model measured: RMSECV: 3.11, RMSEE: 2.05, and RPD: 2.27.

Figure 3-4 shows a series of line plots of the calculated nitrate concentrations as a function of distance away from the plant root for control N (**Figure 3-4A**) and low N (**Figure 3-4B**) growth media. Each point on the plot represents a 100 μm increment. **Figure 3-4A** shows that the plant + fungus plot has the highest nitrate concentration overall, which is present in the first 1500 μm from the plant root. This concentration is approximately 6 times as high as the control concentration (growth media made with 9 mM nitrate) which plateaus near 10 mM nitrate after 1500 μm from the root. The plant-only and plant + bacteria + fungus plots both have twice as much nitrate closer to the root than the control concentration of nitrate. The nitrate concentration for the plant + bacteria plot stays constant at 10 mM over the 3000 μm distance examined.

In **Figure 3-4B**, the plant + bacteria + fungus plot has the highest calculated nitrate concentrations in the distance measured away from the plant root from low N plant samples. The plant + fungus plot has the steepest nitrate gradient in the first 500 μm away from the plant root. The two other conditions, plant-only and plant + bacteria both have a mostly uniform nitrate concentration over the distance measured.

In **Figure 3-5A,** a scatter plot of nitrate and ammonium concentration as a function of distance from the plant root is shown for the plant + fungus sample grown in control N media. The plot shows a high nitrate concentration closest to the plant root, which decreases linearly and

then levels off to ~ 12 mM nitrate after 1500 μm away from the plant's root. The ammonium concentration shows an inverse trend, where the concentration is first low closest to the root, increases, and then levels off to 20 mM ammonium at about 1500 μm away from the plant's root. **Figure 3-5B** shows a scatter plot of nitrate and ammonium concentration as a function of distance from the plant root for the plant + fungus sample grown in low N media. The nitrate and ammonium plots in **Figure 3-5B** follow the same trends described in **Figure 3-5A**, except at lower concentration values. The highest nitrate concentration, which is closest to the plant's root, is ~ 360% and 214% more than the calculated concentration in the non-rhizosphere area in the control N and low N models, respectively. The lowest ammonium concentration corresponds to a 10% and 40% decrease in the calculated concentrations in the non-rhizosphere region in the control N and low N media respectively.
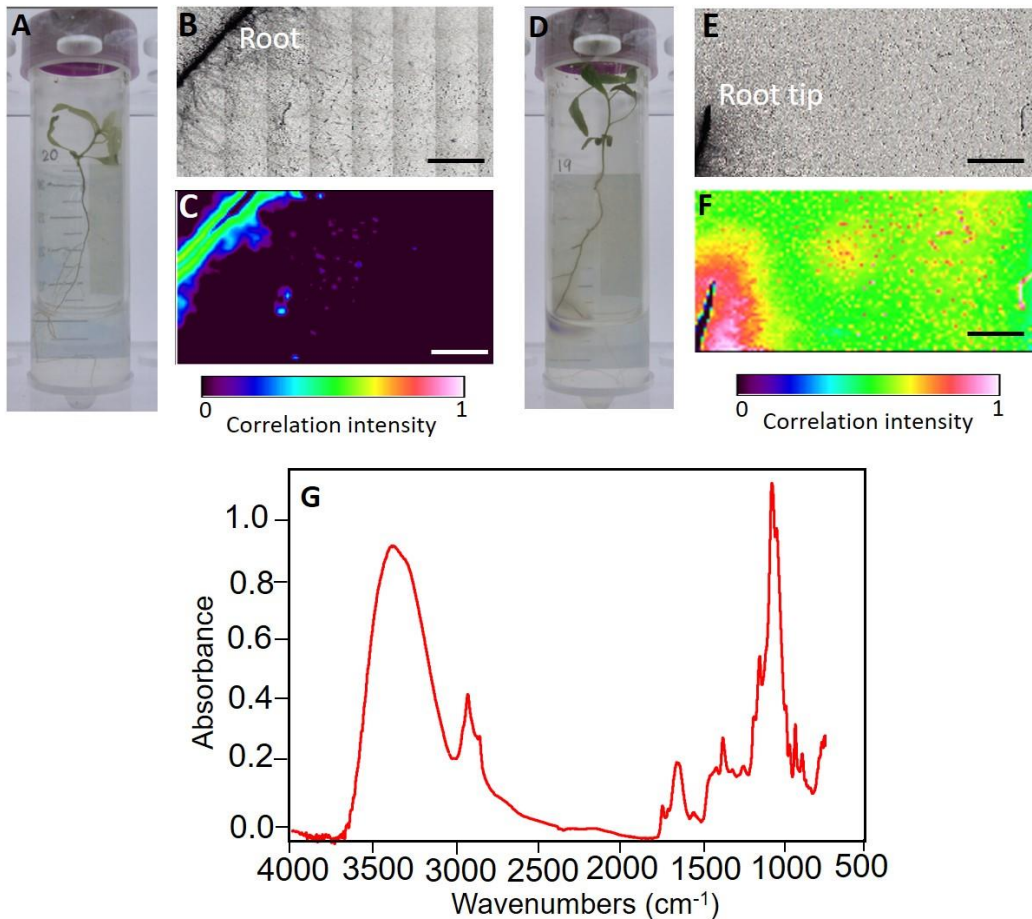
Figure 3-1: A) Poplar plant grown in control N media. **B)** Visible light image of Poplar root tip from **A**. **C)** FTIR image showing the correlation of the fungus, *L. bicolor* in the poplar root tip shown in **B**. **D)** Poplar plant grown with the fungus, *L. bicolor* grown in control N media. **E)** Visible light image showing part of a poplar root from **D**. **F)** FTIR-I image showing the correlation of the fungus, *L. bicolor* in the poplar root section from **E**. **G)** FTIR spectrum of the fungus L. bicolor used to plot the correlation images in **C** and **F**. The plant grown with the fungus in **Figure 1D** grew broader leaves in a larger quantity than the plant which grew without the fungus in **Figure 1A**. The hyphae from the fungus (region highlighted in red) is seen around the root in the plant grown with the fungus in **Figure 1F** but not in the plant grown without the fungus in **Figure 1C**. Scale bar is 100 μm in **Figures B, C, E, F.**
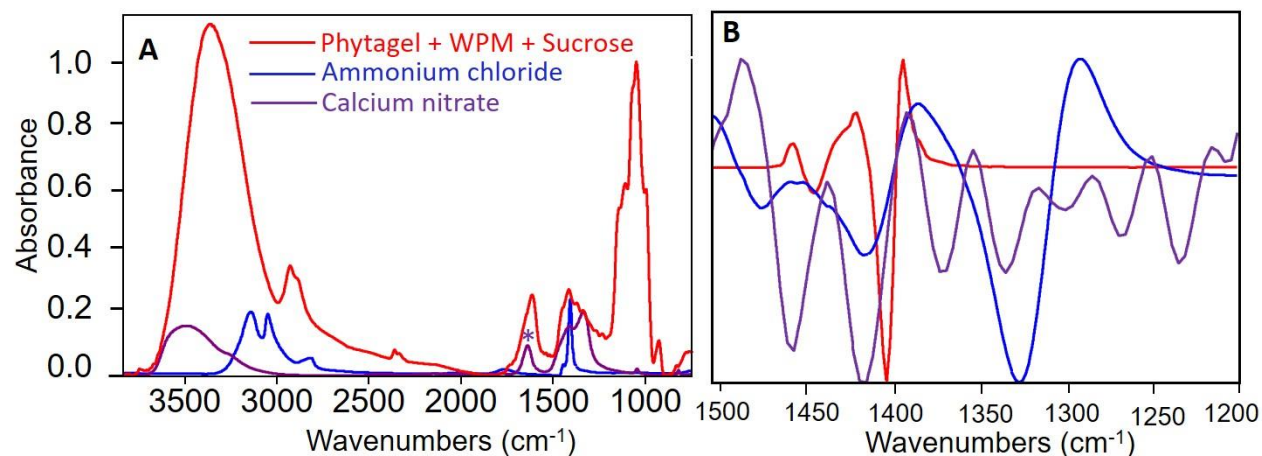
Figure 3-2: A) FTIR spectra of inorganic N sources and the growth media: Phytagel+ Woody Plant Medium + sucrose (red), ammonium chloride (blue) and calcium nitrate (purple) (*hydrate). The ammonium and nitrate bands in the 1300-1500 cm^{-1} region are buried below other components in the growth matrix. **B)** Second derivative spectra of calcium nitrate (purple), ammonium chloride (blue) and Phytagel + Woody Plant Medium + Sucrose (red). In the second derivative spectra, nitrate has three infrared absorption peaks and ammonium has two infrared absorption peaks in the 1300-1500 cm^{-1} region.
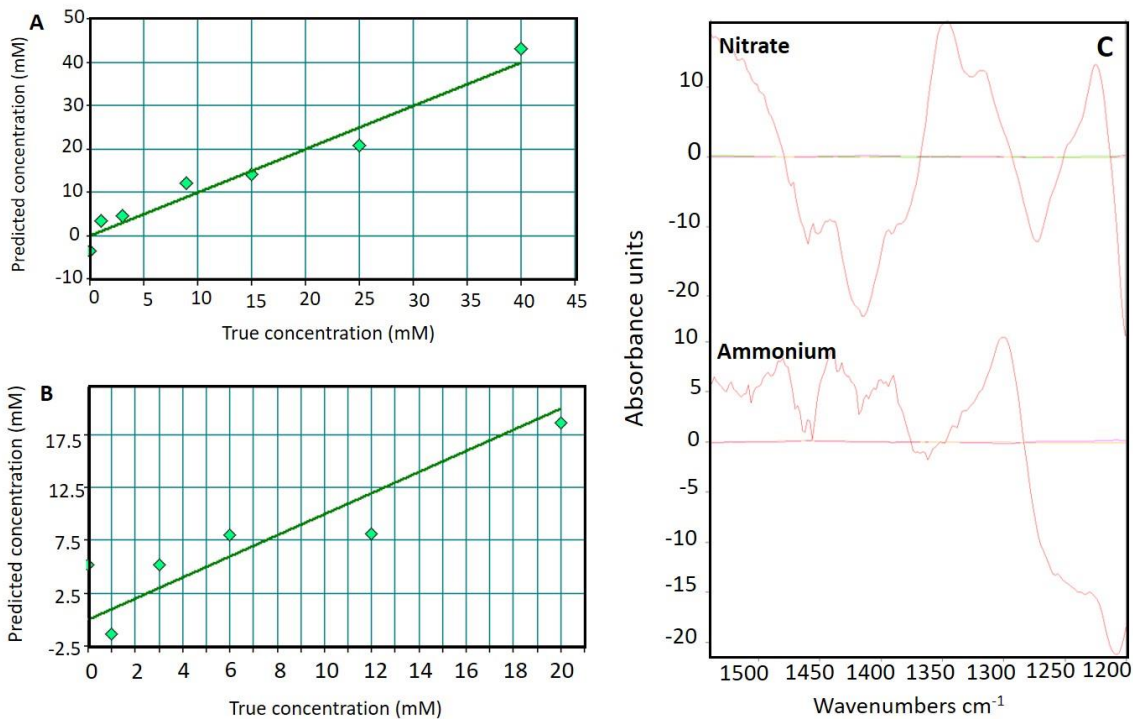
Figure 3-3: Regression plot of measured versus FTIR-predicted values for **A)** Nitrate **B)** Ammonium which were modeled using the 1550 to 1200 cm^{-1} region from the spectra. **C)** Regression spectra showing common wavenumbers that made significant contribution to the modeling of nitrate and ammonium concentrations.
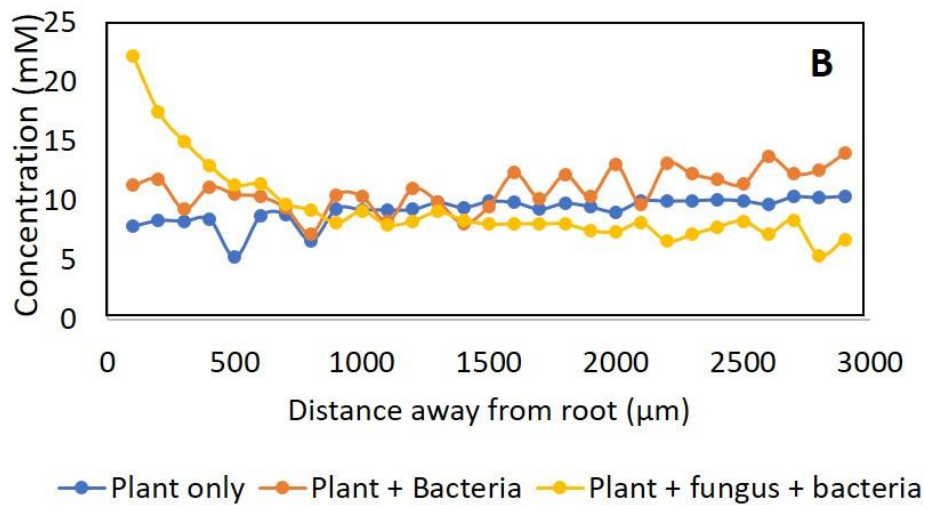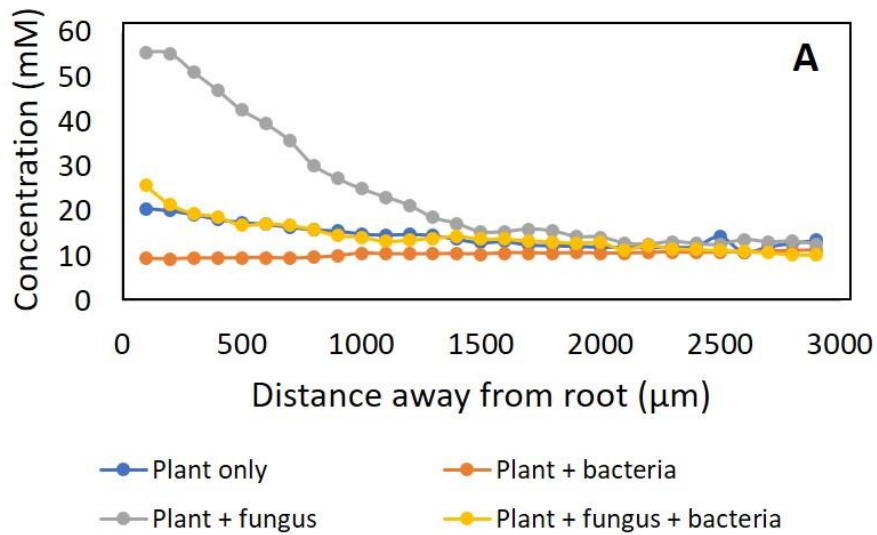
Figure 3-4 Scatter plot of nitrate concentration as a function of distance from the poplar plant root grown with different symbiotic partners in **A)** Control Nitrate and **B)** Low Nitrate. Poplar plants were grown independently, with bacteria, with fungus and a combination of fungus and bacteria.
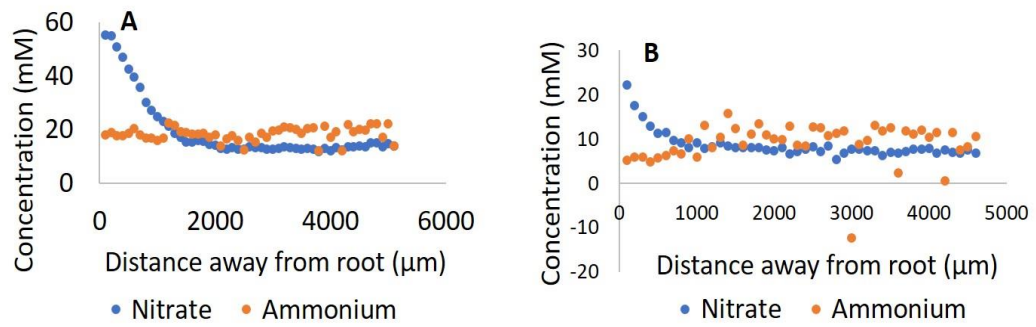
Figure 3-5: Scatter plot of nitrate concentration as a function of distance from the poplar plant root grown with the mycorrhizal fungus, *L. bicolor* in **A)** Control N and **B)** Low N.

Table 3-1: Elements added to plant growth media.

Components	Stock Solutions (g/L)
Sucrose	15
MES	0.5
Phytagel	8
Microelements	
$CuSO_4.5H_2O$	1
FeNaEDTA	36.7
H_3BO_3	6.2
$MnSO_4.H_2O$	22.3
$Na_2MoO_4.2H_2O$	1
$ZnSO_4.7H_2O$	8.6
Macroelements	
$CaCl_2$	72.5
$Ca(NO_3)_2.4H_2O$	556.024
KH_2PO_4	170
K_2SO_4	82.5
$MgSO_4$	180.54
NH_4NO_3	200
Vitamins	
Glycine	2
Myo-Inositol	50
Nicotinic acid	1
Pyridoxine-HCL	1
Thiamine HCL	2

3.5 DISCUSSION

In this study, changes in inorganic N concentrations were monitored using infrared imaging in the rhizosphere of Poplar seedlings grown under different growth conditions. Because the inorganic N sources, nitrate and ammonium, both have infrared absorbance bands in a region dominated by the other components in the growth matrix (mostly Phytagel), it was necessary to use multivariate analysis to predict the concentrations of nitrate and ammonium from the measured samples. To model the data, partial least squares regression was utilized. Several pre-processing and spectra processing combinations were investigated to find the optimum conditions to build the best model. The optimum models chosen had a combination of low error values, low latent values and high R^2 values. The R^2 value is a good indicator of a model (when greater than 0.5) and less PLS components were better to model the data since a model may fit random errors with more components to account for variations in the data.

In this study, three PLS components were chosen to model the nitrate spectra and two latent variables were chosen to model the ammonium spectra. The plot of components used for the nitrate model showed that one of the three components directly corresponded to the nitrate IR vibration at 1340 cm^{-1} while the other two components were indirectly attributed to nitrate changes in the broadening of the peak and changes in peak height at 1225 cm^{-1}. Similarly, the plot of components or latent variables used for the ammonium model showed that one of the two components directly corresponded to the ammonium IR vibration at 1405 cm^{-1} while the other components used was indirectly attributed to ammonium by the peak broadening and peak height changes occurring at 1275 cm^{-1}. The different components which were generated to model the

spectral changes due to nitrate and ammonium infrared vibrations indicate that the PLS algorithm utilized was suitable for modeling the experimental data.

The scatter plots depicting the concentration of nitrate in the rhizosphere showed that the nitrate concentration was highest near the plant's root and decreases away from the plant root in the plant-only, plant + fungus, and plant + bacteria + fungus growth conditions. The mycorrhizal plant + fungus system was able to assimilate the most nitrate at nearly 6 times the control concentration provided in the media. Further than 1500 μm away from the root, the concentration of nitrate remained constant under these three growth conditions. These trends suggest that the nitrate is assimilated into the plant and perhaps stored as N reserves. In the plant + bacteria growth condition, there was no observable nitrate assimilation in the area examined. This is not surprising as plants and fungi are the only eukaryotic organisms able to assimilate inorganic N [68]. The constant nitrate concentration may also indicate that the bacteria concentration was too low to detect any changes in the nitrate concentration, including nitrate consumption. It has been suggested that mycorrhizal fungi first assimilate nitrate from the soil in the extraradical mycelium, then transport the nitrate to the intra-radical mycelium, convert the nitrate into amino acids like arginine and then transfer the amino acid to the host plant via the apoplastic space [69].

A comparison of the nitrate and ammonium concentration in the rhizosphere of the plant + fungus system (**Figure 3-5A**) showed that the ammonium concentration is lower near the plant root and increases away from the plant root, a pattern that is opposite to the nitrate distribution. The trend for the ammonium distribution indicated that the ammonium is consumed while the trend for the nitrate distribution indicates that the nitrate is being assimilated. The type of N a plant utilizes depends on a number of factors including the external N availability, the type of soil, the pH and what amount of N is needed for the growth and functional processes of the plant.

Generally, NH_4 is preferred over NO_3 for consumption by plants because it is energetically more favorable to transport [28].

Under low N conditions, the same nitrate usage pattern was seen by the mycorrhizal fungi (**Figure 3-5B**), where NH_4 is consumed and NO_3 is assimilated. In low N conditions, about 40% of the control concentration of NH_4 is consumed. This percentage is greater than the amount of NH_4 consumed in the control concentration which is approximately 10%. Although the N concentration is ¼ times the control concentration, NO_3 is still assimilated while NH_4 is being consumed. These trends demonstrate that NH_4 is the preferred source for consumption in the plant + fungus system in both high and low N conditions. When nitrate is taken up by the roots it is either reduced, stored in the vacuoles, or translocated to the shoot for reduction and vacuolar storage whereas ammonium is incorporated immediately into amino acids into the roots [70]. This explains why NH_4 is the more favorable choice for consumption and why the percentage of NH_4 consumption increases as the availability decreases as well. Furthermore, plants adapt to changing environmental conditions, e.g low N conditions, by expressing different protein profiles [68].

It has been estimated that approximately 50-70% of all nitrogen provided to the soil is lost [64]. This means that most of the lost nitrogen in the field results in water and soil pollution. To improve nitrate leaching, one of the main goals of plant research is to lower fertilizer input and improve a plant's nitrogen use efficiency (NUE). Given the rising population, and the high costs of producing nitrogenous fertilizers, it is imperative to develop alternative strategies to improve a plant's NUE. We have demonstrated that the mycorrhizal fungus, *L.bicolor* is able to assimilate as much as 60 mM nitrate compared to 20 mM in the plant-only system. This implies

that mycorrhizal fungi may have the potential to be used in improving plant N uptake and hence plant productivity without the use of excess commercial fertilizers.

The use of infrared imaging and multivariate analysis in the work presented showed that it is possible to monitor changes in the inorganic N distribution in the rhizosphere under different growth conditions which can be customized to mimic environmental conditions to select the best conditions (right nutrient source at the right time) to grow plants sustainably.

CHAPTER 4

X-RAY FLUORESCENCE NANOTOMOGRAPHY OF SINGLE CELLS AT 20 NM VOXEL SPATIAL RESOLUTION

4. 1 ABSTRACT

X-ray Fluorescence (XRF) microscopy is a growing approach for imaging trace element concentration, distribution, and speciation in biological cells at the nanoscale. Moreover, three-dimensional nanotomography provides the added advantage of imaging subcellular structure and chemical identity in three dimensions without the need for staining or sectioning of cells. To date, technical challenges in X-ray optics, sample preparation, and detection sensitivity have limited the use of XRF nanotomography in this area. Here, XRF nanotomography was used to image individual *E. coli* bacterial cells at 20 nm voxel resolution, the highest resolution yet achieved with this method. The measurements were performed using nano-Mii (Nanoscale Multimodality Imaging Instrument) at the Hard X-ray Nanoprobe (HXN, 3-ID) beamline at NSLS-II. Cells were embedded in small (5-20 µm) sodium chloride crystals, which provided a non-aqueous matrix to retain the three-dimensional structure of the *E. coli* while minimizing radiation damage. Results showed the distribution of calcium, potassium, sulfur, phosphorus, iron, and zinc with sufficient resolution to visualize cell membranes. This work demonstrates that XRF nanotomography can be performed on unfrozen biological cells to co-localize elemental distribution at 20 nm voxel spatial resolution.

4.2 INTRODUCTION

Trace elements are essential for carrying out biochemical reactions and act as structural components in cells. The appreciation of the important roles that trace elements, especially metals, play in cell metabolism has caused an increase in the number of studies of this area [71]. However, to truly understand the function of trace elements in cells and tissues, the distribution within a cell must be imaged and quantified in the native cellular environment, which has proven to be difficult.

Hard X-ray Fluorescence Microscopy (XFM) is a well-suited microanalytical technique for assessing the elemental distribution in a wide range of materials and biological samples including whole cells and tissue sections [72-74]. In XFM, multiple elements can be mapped simultaneously, which provides precise elemental co-localization and speciation. High detection sensitivity down to sub-parts-per-million has been demonstrated for biological studies [75, 76].

To understand the functions of trace elements in biological cells, an X-ray probe must resolve subcellular compartments on the sub-micron to nanometer scale such as mammalian nuclei, mitochondria, and cell membranes, which measure 6 μm, 1 μm and ~10 nm, respectively [77], as well as prokaryotic cells such as *E. coli* (1 μm x 3 μm). Nanoscale imaging with X-rays requires high-resolution nano-focusing optics [78, 79], an extremely stable environment to minimize vibrations, and stiff components to reduce thermal drift [80]. It becomes even more challenging to investigate biological specimens due to the potential for radiation-induced damage. To mitigate this, cells are often imaged in the dried or frozen-hydrated state [81]. Furthermore, since the trace elements are typically micro- to nanomolar in concentration, sensitive detectors with large solid angle are required for quantification.

Whereas two-dimensional XRF microscopy analysis works well for thin sections of cells and tissues, these two-dimensional data can be ambiguous when imaging three-dimensional objects especially when aiming to differentiate between elements located on the surface of a cell from those distributed throughout the cell. At present, only a few three-dimensional XRF tomography studies from whole biological specimens have been reported. Kim *et al*. have studied the role of the vacuolar iron uptake transporter in the uptake and distribution of iron in the *Arabidopsis* seed, which was performed at 12 μm spatial resolution [82]. More recently, de Jonge *et al*. performed three-dimensional XRF tomography of a whole diatom, *Cyclotella meneghiniana*, at 400 nm spatial resolution using 150 nm voxels over a 15 μm field of view [73]. This work elegantly shows the distribution of several species including silicon and zinc within the organelles including the siliceous frustule, a diatom's cell wall. Most surprising was the detection of Fe and Mn rings in the cell wall that would not have been detectable using only two-dimensional projections.

To date, XRF microscopy studies have been limited to sub-micron spatial resolution and weak absorption contrast in biological cells, inhibiting its ability to distinguish the ultra-structures of cell organelles [83]. In contrast, coherent diffraction imaging techniques, like ptychography, can be used to image the fine structural components in samples [84], but cannot determine the distribution of trace metals. However, by combining XRF nanotomography and ptychography, it is possible to obtain complementary data on structural and elemental composition in nanoscale structures from biological cells [74, 85]. The results described here represent combined XRF nanotomography and ptychography performed on *E. coli* cells at 20 nm voxel spatial resolution - the highest spatial resolution yet achieved using hard X-rays on a biological specimen.

4.3 METHODS

4.3.1 CELL CULTURE

LB media (10 mL) was inoculated with a single colony of BL21 (DE3) *E. coli* cells and the culture grown at 37 ℃ (shaking) to an OD of 0.6-0.8. Cells were treated with 1 mM isopropyl β-D-1-thiogalactopyranoside and grown for an additional 4 hrs, with shaking at 37 ℃. Cells were harvested in 1 mL aliquots via centrifugation at 3,500 RPM, flash frozen in liquid nitrogen, and stored at -80℃.

4.3.2 SAMPLE PREPARATION, LIGHT MICROSCOPY AND SCANNING ELECTRON MICROSCOPY

A 20 μl solution containing 0.4 mM NaCl, 0.01 OD *E. coli* cells and 0.025 OD 100 nm gold nanoballs (CytoDiagnostics, sample # GRF-100-20) was mixed thoroughly. The gold nanoballs were added as fiducial markers for the tomography reconstruction. One microliter of this solution was pipetted onto a silicon substrate, also known as a "diving board" (substrate area 1.5 mm by 0.5 mm, membrane thickness 10 μm), and allowed to dry overnight. The diving board was then glued onto a stainless-steel insect pin (0.2 mm thick, 16.5 mm tall) and mounted on the sample mount for the X-ray microscope, **Figure 4. 1**. **Figure 4.1D** shows the Si substrate next to a US penny to depict relative size. The diving board has platinum patterned gridlines for sample alignment in the X-ray microscope. Images of samples mounted on the diving boards were taken using both a visible light microscope (Nikon Eclipse LVDIA-N) and a scanning electron microscope (JEOL 300) for cell identification, correlation, and navigation during data acquisition at the beamline.

4.3.4 SYNCHROTRON X-RAY FLUORESCENCE MICROSCOPY MEASUREMENTS

The distribution of elements was mapped using nano-Mii (Nanoscale Multimodality Imaging Instrument) at beamline 3-ID (HXN) at the National Synchrotron Light Source II (**Figure 4.1A**). Beamline 3-ID provides a scanning X-ray microscope capable of multimodal imaging including absorption, fluorescence, differential phase contrast, and ptychography. In this study, a 12 keV incident beam was focused to a 15 nm spot using multilayer Laue lenses (MLLs) for XRF mapping. Two-dimensional fluorescence scans, via continuous fly-scan, were performed using a step size of 20 nm/pixel and a dwell time of 250 ms. For the tomography data set, the cells were scanned over ± 70 degrees at 3 degree intervals using a dwell time of 100 ms and a 20 nm/pixel step size.

The fitting of the X-ray fluorescence data was accomplished using PyXRF, an X-ray fluorescence analysis package developed at NSLS-II [86]. TomoPy was used for the tomography reconstruction of the data sets [87]. The ptychography reconstruction was conducted with 200 iterations of a difference map algorithm. A 96×96 pixel array was cropped from the raw experimental data for ptychography reconstruction, which gave a 10 nm pixel size in the obtained real-space image. The illumination function was characterized with a test pattern before imaging the cellular specimen. The transmission function of the cell was initialized as a randomized complex array. A typical reconstruction converges within 20 iterations, and the last 40 iterations were averaged to give the final image.

4.4 RESULTS

E. coli cells were mounted on the silicon substrate and examined under an optical light microscope in epi-brightfield mode followed by visualization using a scanning electron microscope (SEM). The SEM image (**Figure 4.2A**) displays *E. coli* cells (typically 1 μm x 3 μm in size) embedded in small sodium chloride crystals (1-20 μm) that formed on the silicon substrate, where the cells appearing as dark (negative contrast) regions in the crystals. The inset in **Figure 4.2A** shows a magnified view of a group of cells lined up side-by-side within a sodium chloride crystal.

Two-dimensional elemental images (**Figures 4.2B-E)** were taken using XRF microscopy, mapping the distribution and co-localization of zinc, calcium, and chlorine. All elements analyzed were detected by their K-alpha lines. The chlorine image (**Figure 4.2D**) shows the location of the sodium chloride crystals and the dark regions indicate the areas occupied by the cells embedded in the crystal, which correlates well with the SEM image in **Figure 4.2A**. Notably, zinc exhibits an inhomogeneous distribution (**Figure 4.2B**) whereas a uniform distribution of calcium (**Figure 4.2C**) is observed throughout the cell.

In **Figure 4.3A**, the two-dimensional zinc distribution is shown in another series of cells. Again, the distribution of zinc is uneven within the cells and varies from cell to cell. The gold elemental map (**Figure 4.3B**) was used to localize the gold nanoballs which were added to the cell solution as fiducial markers for the alignment and reconstruction of the tomography data. These gold nanoballs are also obvious in the ptychography reconstructed phase image (**Figure 4.3C**) along with the clear outline of two cells that appear to be dividing.

The zinc distribution was further analyzed in a series of zinc projections from a three-dimensional XRF nanotomography dataset of a single *E. coli* cell (**Figure 4.4**). Similar to the 2D

data, the tomography projections show that zinc is in homogeneously distributed throughout the

cell. But in addition, the 3D projections show that Zn is localized in the cell membrane and is

more heavily concentrated at one pole of the cell.
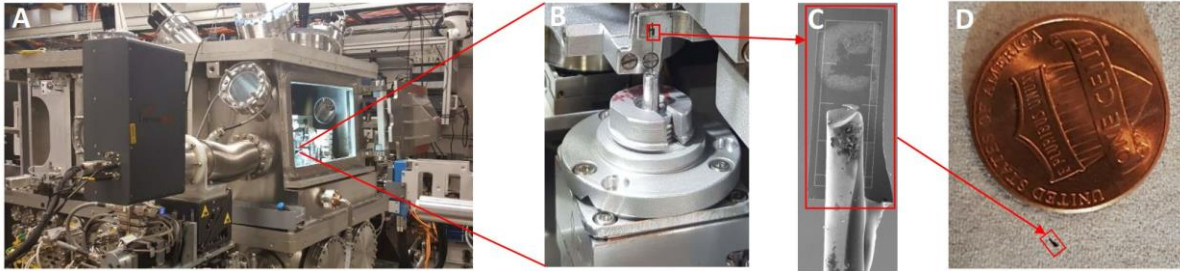
Figure 4.1: (A) X-ray Microscope at the Hard X-ray Nanoprobe (HXN, 3-ID) beamline at
NSLS-II **(B)** Sample mounted on the rotation stage for tomography **(C)** *E. coli* bacteria
deposited on a Si substrate ("diving board") that was mounted to an insect pin **(D)** Size
comparison between the Si substrate and a US penny. Substrate is 1.5 x 0.5 mm.
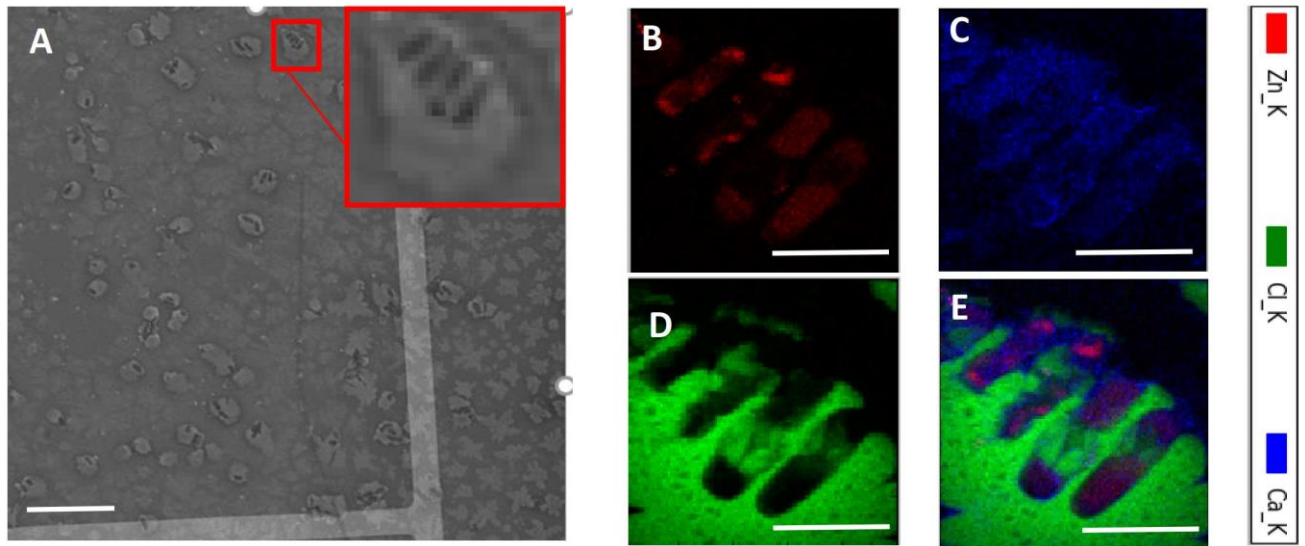
Figure 4.2: (A) SEM image showing *E. coli* bacteria embedded in NaCl crystals on the HXN Si sample holder with Pt-patterned fiducial grids. Cells appear as dark (negative contrast) regions in images. Scale bar is 20 μm. XFM image showing **(B)** zinc, **(C)** calcium, **(D)** chlorine distributions in *E. coli* cells. **(E)** XFM image showing co-localization of zinc, calcium and chlorine in *E. coli* cells. Scale bar is 2 μm in B, C, D, E.
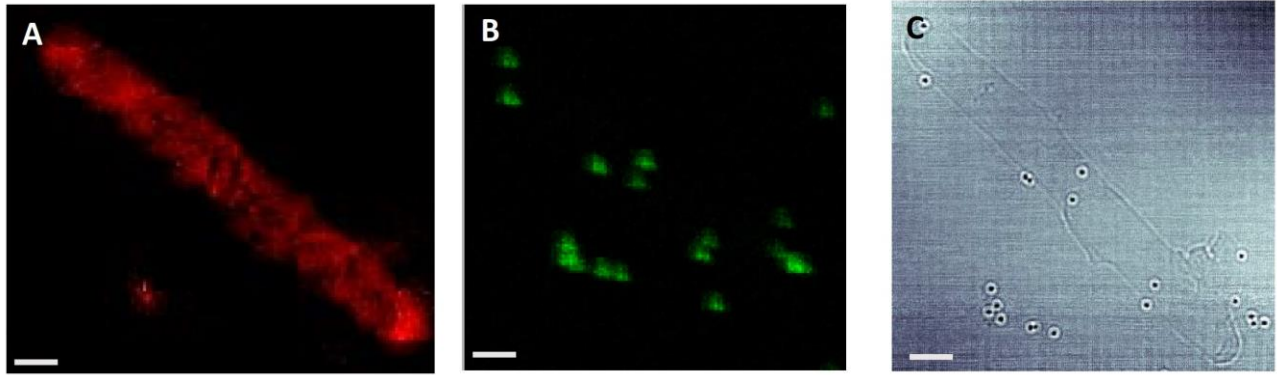
Figure 4.3: XRF microscopy images showing the **(A)** zinc and **(B)** gold distribution in several *E. coli* cells lined up end-to-end. **(C)** Ptychography reconstructed phase image of the cells from **(A)** showing the cell boundaries and the 100 nm gold nanoballs that were added to the cell solution as fiducial markers for alignment and tomography reconstruction. Scale bar is 1 μm.
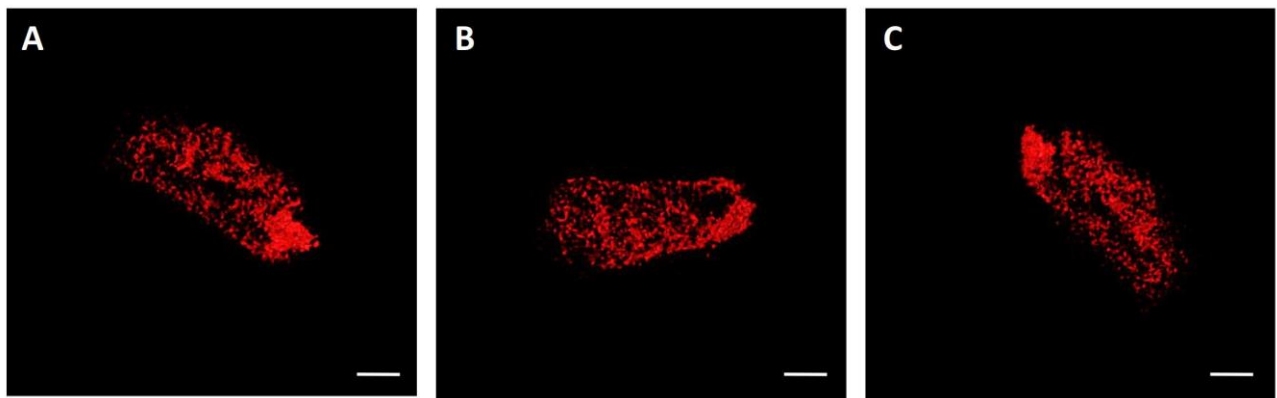
Figure 4.4: Projections from the XRF nanotomography reconstruction of an *E. coli* cell showing the zinc distribution in different orientations. The images show that zinc is inhomogeneously distributed throughout the cell, more heavily distributed at one pole, and has an elevated distribution at the outer membrane compared to the cytosol. Scale bar is 500 nm.

4.5 DISCUSSION

In this study, we performed X-ray fluorescence microscopy, nanotomography, and ptychography on individual *E. coli* cells at 20 nm spatial resolution. The distributions of phosphorus, sulfur, calcium, iron, copper, and zinc were imaged, focusing on the sub-cellular distribution of zinc. Tomography results showed an inhomogeneous zinc distribution in the cell presented, with a higher concentration at one pole. Most of the internal labile zinc is thought to be stored in the ribosomes [88-90]. Generally, ribosomes are distributed among and around the central nucleoid, a highly condensed, irregular structure containing the genetic material of the bacterial cell [91, 92]. This ribosome distribution leads to ribosome-rich regions especially at the polar end-caps of the cell and in a cylindrical shell surrounding the nucleoid [91] which would explain the high amounts of zinc observed in these regions here [89, 90, 93]. In rapidly growing *E. coli, it is believed that the* majority of the translation events are presumably carried out on mature, freely diffusing mRNAs within this localized ribosome-rich, "protein-factory" region using poly-ribosomes [94]. In bacteria, zinc can play a structural, regulatory, or catalytic role in proteins and is tightly controlled by dedicated systems for high-affinity zinc uptake and export systems involving the cell membranes [90, 95]. All gram-negative bacteria, like *E. coli*, possess an outer membrane, a periplasmic space, and an inner cytoplasmic or plasma membrane through which the metal must pass before entering the cytosol [95, 96]. Zinc homeostatic proteins move metal ions or small-molecule metal chelators across these otherwise impermeable barriers in a directional fashion. Hence, zinc transport across the cell membrane and into the cell is likely to result in a localized zinc content at the cell surface, as observed in this work.

Having the ability to assess the zinc distribution in the cell membrane and cytosol of *E. coli* – as is possible with XRF nanotomography – is essential for establishing the role of zinc in cellular processes and disease. Importantly in bacteria, infectivity can readily be altered by varying levels of zinc in the host system [97]. More broadly, zinc plays a vital role in the physiology of all organisms and its homeostasis is widely studied in areas such as aging, neurodegenerative diseases, cancer, the immune system, and energy metabolism.

This work represents one example of how XRF nanotomography and ptychography can be used to investigate trace elements in biological cells and tissues. It was made possible through the development of a high brightness synchrotron source, nanofocusing optics, and exceptional beam and sample stability. One of the limitations of nanoscale X-ray imaging of biological samples is the inherent radiation damage that occurs with hard X-ray exposure, which can change the structure and chemistry of samples. Typically, cryofixation is used to mitigate these effects. In this study, we were able to image bacteria nondestructively at room temperature by embedding the cells in small (5-20 µm) sodium chloride crystals. This simple and straightforward approach provided a non-aqueous matrix to retain the three-dimensional structure of individual cells. Furthermore, the XFM and SEM contrast provided by chlorine greatly enhanced the ability to locate individual cells on the sample substrate, also minimizing the radiation dose acquired. While this method may not be applicable to all cells, it is likely to be effective for many simple cell types including bacteria, archaea, and algae.

In summary, this study demonstrates that XRF nanotomography can be used to image the distribution of trace elements in whole biological cells at 20 nm spatial resolution in three dimensions, and simultaneous ptychography aids in the co-localization of the trace elements with subcellular structures. An approach such as this presents new possibilities in understanding

subcellular biochemistry in individual organelles and other subcellular compartments, which are usually analyzed at the organelle population level.

CHAPTER 5

LANTHANIDE-BINDING TAGS (LBTS) FOR NANOSCALE X-RAY IMAGING OF PROTEINS IN CELLS AND TISSUES

5.1 ABSTRACT

X-ray Fluorescence Microscopy (XFM) is becoming a widespread and powerful method for imaging trace element concentration, distribution, and speciation in biological cells and tissues at the nanoscale. However, one limitation of XFM for imaging biological systems is detecting the trace-element distribution in the context of subcellular organelles and individual proteins. For visible light microscopy, the most ubiquitous method for imaging individual proteins within the context of a living cell is the use of intrinsically fluorescent proteins, such as the green fluorescent protein (GFP) that is co-expressed as a fusion tag along with the protein of interest. However, visualization of these tags with optical microscopy is limited by the wavelengths of visible light except by applying specialized super resolution approaches. Here, applications enabled by encoded lanthanide-binding tags (LBTs), which are GFP-like analogs of minimal size (ca. 15-20 amino acids) have been developed for XFM. The LBTs can enable better than 10 nm spatial resolution imaging of individual proteins in cells and tissues while simultaneously obtaining trace-element distribution throughout the cell.

5.2 INTRODUCTION

X-ray Fluorescence Microscopy (XFM) is a unique method for imaging trace-element concentration, distribution, and speciation in biological cells and tissues [98]. Recent advances in X-ray sources, optics, and detectors are enabling three-dimensional imaging at the nanoscale with attogram detection sensitivity [99]. However, one major limitation of XFM is understanding and controlling the trace-element distribution in the context of subcellular organelles and individual proteins. Traditionally, visible light microscopy is the most ubiquitous method for imaging individual proteins within the context of a living cell where fluorescent proteins such as the green or yellow fluorescent protein (GFP or YFP, respectively) are co-expressed as a fusion tag attached to the protein of interest. However, visualization of these tags is limited by the wavelengths of visible light except by applying specialized super resolution approaches. In addition, the GFP/YFP fusion tags are large proteins themselves (~27 kDa), which can easily alter the expression, localization, function, and transport of the parent protein of interest.

In order to address these limitations, lanthanide-binding tags (LBTs) have been utilized as a GFP-like analog for XFM that have the potential to enable <10 nm spatial resolution imaging of individual proteins within cells and tissues. Unlike GFP, these tags are short peptides (15-20 amino acids) comprised almost entirely of a nanomolar-affinity lanthanide-binding domain. The LBTs can be easily incorporated into the target protein sequence, and their small size minimizes any deleterious effects on target protein expression, function, or transport within the cell. Moreover, LBTs can be lanthanide-specific, opening the possibility of tagging multiple proteins simultaneously. Thus, these unique characteristics of LBTs provides the flexibility to label many sizes and types of proteins within the cell. The high affinity of the LBTs for

lanthanides means that experiments can be performed at low concentrations of Ln ions which appears to mitigate toxic effects.

Since lanthanides are not naturally present in cells, LBTs are an excellent element-specific (and hence protein-specific) tag for XFM. Here the use of LBTs to image a membrane protein on the surface of an *E. coli* cell, and the distribution of dLBT-ubiquitin within the bacterial cytosol was demonstrated. Results show that both Eu-LBTs and Er-LBTs can be visualized in both two- and three-dimensions at a spatial resolution of ~20 nm. These findings suggest that LBTs could become a widespread tool for 3D imaging of individual proteins within cells with a high spatial resolution while simultaneously obtaining trace element distribution.

5.3 METHODS

5.3.1 SAMPLES AND PREPARATION

In this study, LBTs were co-expressed with an outer membrane protein (OmpA) and a cytosolic protein (ubiquitin) in *E. coli* bacteria. One of the four extracellular loop regions of OmpA (residues 106-114) was targeted for LBT insertion. In the case of ubiquitin, the LBT is at the N-terminus. For negative controls, the same expression vectors were produced encoding the OmpA or ubiquitin proteins without the LBT.

OmpA was expressed in SoluBL21 *E. coli* cells to $OD_{600} = 0.6$-0.8 and induced with 1 mM IPTG for 3 hours. Cells were harvested by centrifugation and resuspended in wash buffer (1 mL) containing 150 mM NaCl to remove excess phosphate. Cells were washed three times, resuspended, and incubated for 15 min in 150 mM NaCl with 5 μM $EuCl_3$ or $ErCl_3$. The cells were then washed again (3x) with wash buffer to remove unbound lanthanide ions.

The dLBT-ubiquitin was expressed in BL21 DE3 *E. coli* cells to OD_{600} = 0.6-0.8 and induced with 1 mM IPTG for 3 hours. $EuCl_3$ or $ErCl_3$ (1 mM) was added following induction. Cells were harvested by centrifugation. Cells were then resuspended and washed 3x in 1 mL of 150 mM NaCl to remove phosphate and excess lanthanide ions.

Eu-LBT and Er-LBT were chosen for these experiments since the L_3 edge emission of Eu ($L_{\alpha 1}$ = 5848 eV) and Er ($L_{\alpha 1}$ = 6948 eV) have the least overlap with other exogenous elements in the cell, most notably Fe (K_α = 6404 eV). Er and Eu have similar affinities for the LBTs, and similarly low toxicity.

Once the cells were prepared and washed, they were spun down to a loose pellet, resuspended into a 150 mM solution of NaCl, and a 1 µl aliquot was pipetted onto a HXN-specific silicon nitride membrane (1.4 mm x 0.5 mm, 10 µm thick), and allowed to dry. At this concentration of NaCl, the *E. coli* cells become embedded in salt crystals, preventing them from collapsing (i.e. flattening) on the substrate surface. The NaCl matrix provides a nonaqueous medium to retain the 3D structure of the *E. coli* while minimizing radiation damage without the need for cryofixation.

Cells expressing either OmpA or ubiquitin were exposed to either 50 µM lanthanide chloride (for extracellular binding to OmpA) or to 100 µM or 1 mM lanthanide chloride (intracellular binding to ubiquitin) in the following conditions: (1) Protein only, no lanthanide, no LBT; (2) Protein+LBT, no lanthanide; (3) Protein+ lanthanide, no LBT; (4) Protein+LBT+lanthanide.

5.3.2 DATA COLLECTION:

Cells were deposited on a Si substrate, which was 0.5 mm x 0.2 mm x 10 µm thick and patterned with 5 µm-wide Pt bars as fiducial markers for identifying the location of the beam on the substrate. All samples were prescreened with Transmission Electron Microscopy (TEM) to identify the locations/coordinates of all the cells. It should be noted that TEM prescreening with Kapton polyimide or silicon nitride substrates was not possible due to charging effects from these non-conductive substrates.

X-ray Fluorescence Microscopy was performed at the Hard X-ray Nanoprobe beamline 3-ID at the National Synchrotron Light Source II (NSLS-II) at Brookhaven National Laboratory and the Bionanoprobe beamline 21-ID at the Advanced Photon Source at Argonne National Laboratory. At 3-ID, experiments were performed with a monochromatized energy fixed above the Zn K-edge at 12 keV. The beam was focused with MLLs to ~15 nm in size. An energy-discriminating, three-element silicon drift detector was oriented at 90° from the incident X-ray beam direction to collect the X-ray fluorescence signal. Tomographic datasets were obtained using projection images of 100×80 pixels at 20 nm pixel size and a dwell time of 100 msec per pixel, over a rotation angle range of -66° to 109° at 3° increments. Phase contrast and ptychography images were also collected from the same samples to help identify cell edges and subcellular structures.

At 21-ID, experiments were performed using a double-crystal Si [33] monochromator to produce 10 keV incident X-rays, and a Fresnel zone plate to produce a focus spot with a resolution of ~85 nm. An energy-discriminating, single-element silicon drift detector was oriented at 90° from the incident X-ray beam direction to collect the X-ray fluorescence signal. Tomographic datasets were obtained using projection images of 70×92 pixels at 50 nm pixel size and a dwell time of 100 msec per pixel, over a rotation angle range of -72° to 66° at 3° increments.

5.3.3 DATA ANALYSIS:

The element-specific images were generated with either MAPS (APS) or pyXRF (NSLS-II). Each pixel was fitted and the concentrations of Cl, Ca, Fe, Cu, Zn, Eu, and Er were determined. The open-source and documented package TomoPy [87] was used for the reconstruction and reprojection of the datasets.

5.4 RESULTS

In this study, Eu- and Er-LBTs bound to a membrane protein, OmpA, and a cytosolic protein, ubiquitin were imaged. Cells were embedded in small NaCl crystals, which we have found to retain the three-dimensional shape and minimize radiation damage. In addition, the cells provide a negative contrast in the Cl XRF image, making them easy to identify. **Figure 5-1** shows the XFM images of the Cl, Ca, Zn, and Eu distribution in a cluster of five *E. coli* cells, where OmpA was tagged with 5 μM Eu-LBT. The cells can clearly be visualized in the Cl image (**Figure 5-1A**), where they are seen as negative density among the NaCl crystals.

The Ca and Zn images (**Figures 5-1B, 5-1C**) show that these elements are inhomogeneously distributed in the cells. In particular, the Zn concentration is localized at the polar end caps of the cells. Zinc distribution is typically associated with the ribosomes, which are typically located at the polar end caps of the cells [89-91, 93].

The Eu image (**Figure 1D**) also shows that this element is inhomogeneously distributed, where Eu is most highly concentrated near the surface of the cells. Unlike the other endogenous elements in the cells, Eu is only expected to be associated with the LBT. In this case, the Eu-LBT is bound to an extracellular loop of OmpA. Hence the XFM image is consistent with a membrane-bound Eu-LBT. It should be noted that a few of the cells show Eu density within the

cell, which was not expected to be the case. However, the possibility of non-specific Eu binding/uptake is possible. In particular, if a cell is apoptotic, membrane permeabilization can occur, resulting in diffusion of the Eu ions into the cell.

Lanthanides have been shown to block Ca channels in cells, and also to be transported into cells via ion channels [100]. Since this would contribute to background (i.e. non-specific) uptake of the lanthanides into the cells, the *E. coli* exposed to Eu without the LBT was examined. **Figure 5-2** shows the Cl, Ca, Zn, and Eu distributions within these control cells. The Cl image in **Figure 5-2A** clearly shows the location of the cells and the Ca and Zn images (**Figures 5-2B, 5-2C**) show a similar heterogeneous distribution as seen in **Figure 5-1**. However, the Eu image (**Figure 5-2D**) does not show any uptake of the lanthanide into the cells. Hence, if the ion channels are transporting Eu into the cells, it must be occurring at a very low level.

LBTs can be used to visualize membrane proteins both on the exterior surface of cells and in the cellular cytosol. Here, Eu-LBT was fused to ubiquitin in *E. Coli* (**Figure 5-3**). In **Figures 5-3A-D**, the distributions of Cl, Ca, Zn, and Eu can be seen. Similar to the OmpA-LBT images, the location of the cells within the NaCl crystals can be seen in the Cl image (**Figure 5-3A**). Ca and Zn are heterogeneously distributed in the cells; Eu is more uniform, which is consistent with the fact that ubiquitin is expressed throughout the cell [101].

In the absence of the LBT on the ubiquitin, there was no evidence of Eu uptake into the cells (**Figure 5-3E-H**). This was further confirmed by examining the energy dispersive spectrum from the ubiquitin experiments. When dLBT-Ubi was exposed to 1 mM Eu, distinct X-ray fluorescence peaks are shown at 5.85 keV ($L_{\alpha 1}$) and 6.46 keV ($L_{\beta 1}$). Without the tag, the Eu fluorescence peaks are absent. These results indicate that the LBTs can be transported into the cell in sufficient quantity in order to bind the LBT.

The design of LBTs is such that the binding site can accommodate a range of lanthanides, all with nanomolar affinity [102, 103]. For X-ray fluorescence microscopy of biological cells and tissues, it is important to choose a lanthanide that does not have fluorescence emission lines that overlap with the trace element(s) of interest. Eu is one such lanthanide, as can be seen in **Figures 5-1 to 5-3**. Erbium, which does not overlap with the biologically essential trace elements including Mn, Fe, Cu, and Zn was also tested. **Figure 5-4** shows the visible light image and the XFM images of Ca and Er in a cluster of six cells expressing dLBT-Ubiquitin and incubated with 1 mM Er. The Ca image shows that Ca is distributed uniformly in each cell. Er was also uniformly distributed but, interestingly, it was only present in one of the cells, suggesting that expression of dLBT-Ubiquitin was incomplete in this experiment.

In addition to two-dimensional nanoscale imaging, LBTs can also be used to visualize proteins in cells in three dimensions. Tomography is particularly important for imaging at the nanoscale, especially for applications such as membrane proteins. **Figure 5-5** shows the X-ray nanotomography image of a single LBT-OmpA *E. coli* cell that was incubated with 5 µM Er. The image confirms the 2D data in **Figure 5-1** that the lanthanide is primarily located on the surface of the cell. It is not uniformly distributed on the surface; instead it has a patchy configuration. Since OmpA is known to be a porin-like integral membrane protein [104], this could be a physiological effect such as the formation of lipid rafts or other supramolecular structures in the membrane for signaling or transport.
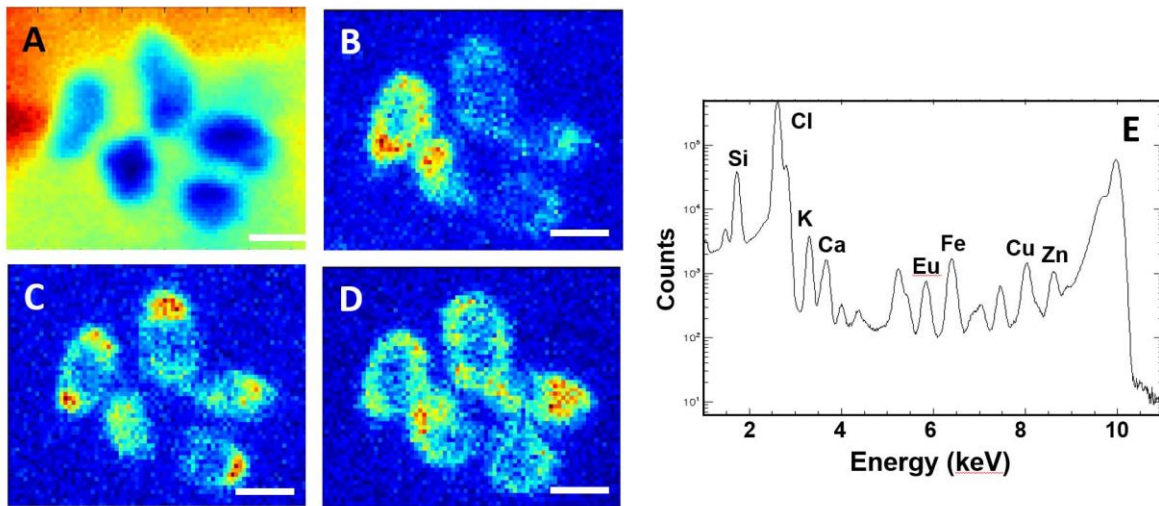
Figure 5-1: XFM images showing the distribution of **(A)** Cl, **(B)** Ca, **(C)** Zn, and **(D)** Eu in *E. coli* cells tagged with OmpA-LBT. **(E)** The energy-dispersive spectrum of all pixels in the map. The Eu fluorescence is clear from the peak at ~6 keV. Scale bar is 2 microns.
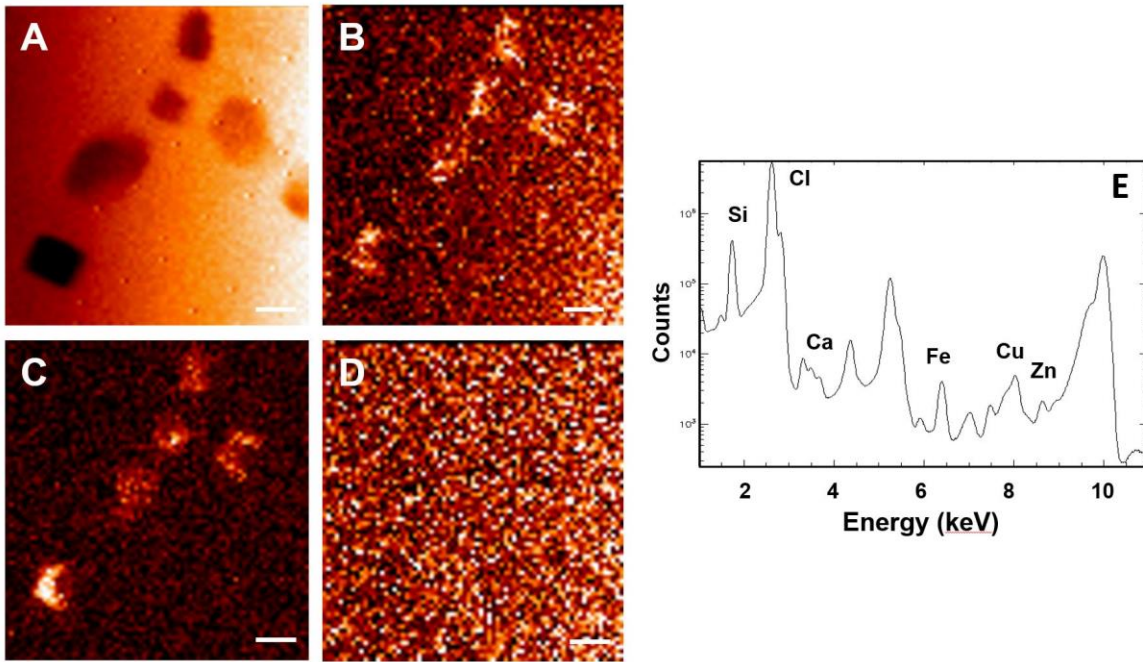
Figure 5-2: XFM images showing the distribution of **(A)** Cl, **(B)** Ca, **(C)** Zn, and **(D)** Eu in *E. coli* cells exposed to Eu without the LBT. **(E)** The energy-dispersive spectrum of all pixels in the map. Scale bar is 2 microns.
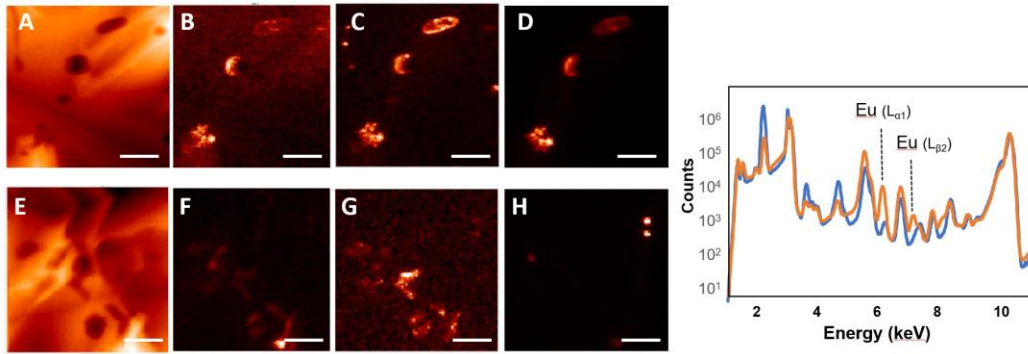
Figure 5-3: XFM images showing the distribution of **(A, E)** Cl, **(B, F)** Ca, **(C, G)** Zn, and **(D, H)** Eu in E. coli cells incubated with Eu with Ubiquitin-dLBT (A-D) and without the LBT **(E-H)**. **(E)** The energy-dispersive spectrum of all pixels in each map. Scale bar is 2 microns.
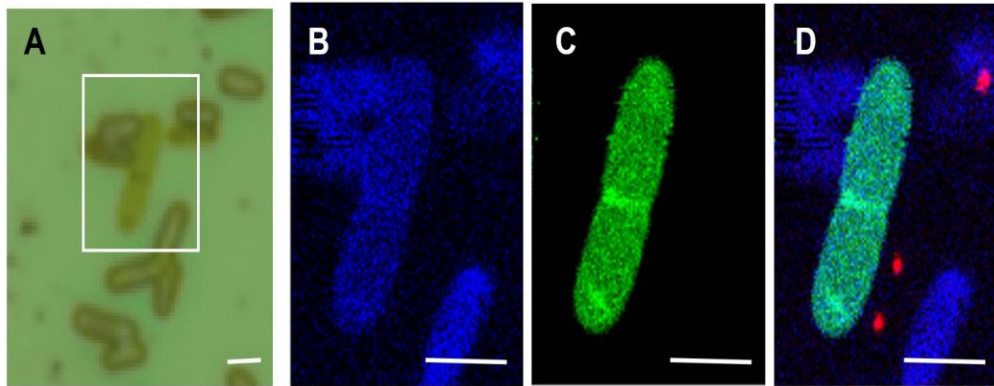
Figure 5-4: (A) Visible light microscopy, **(B)** Ca XFM, **(C)** Er XFM and **(D)** Merged XFM of Ca (blue), Er (green) and Au (red) images of five *E. Coli* cells tagged with Ubi-LBT and incubated with 1 mM Er. 100 nm Au nanoballs are seen in red in (D) Scale bar is 2 microns.
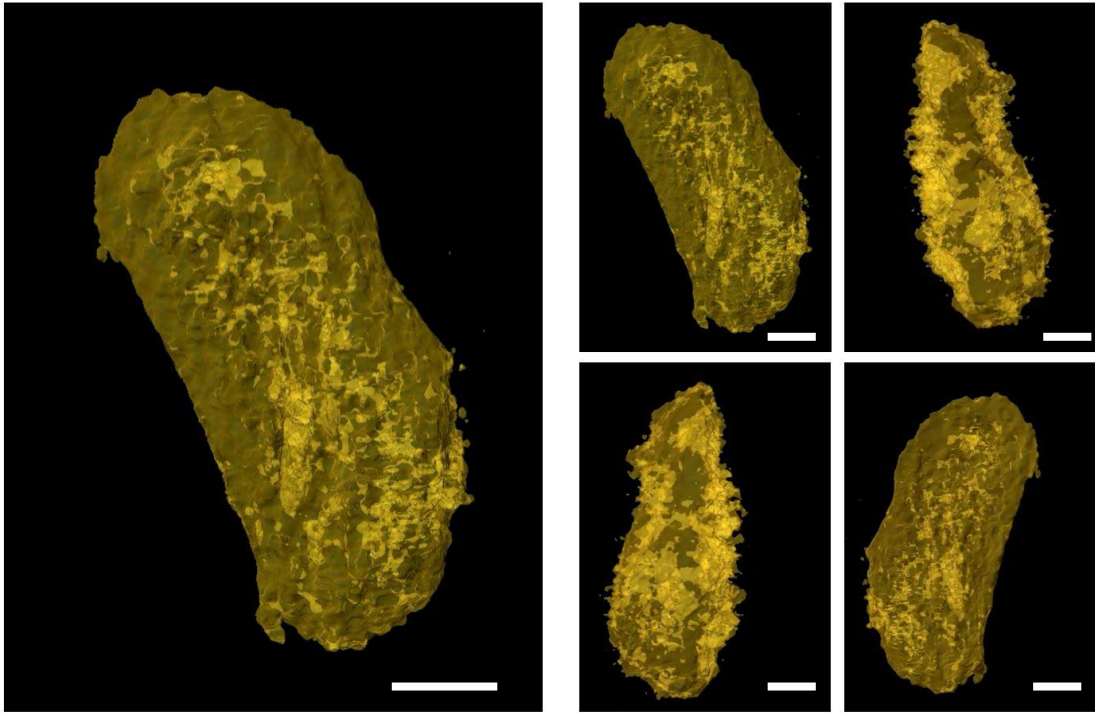
Figure 5-5: X-ray fluorescence nanotomography of a single *E. coli* bacterium expressing OmpA-LBT and incubated with Er. (Left) 3D tomogram and (Right) four projections from the tomogram showing the distribution of Er in the cell. The Er is located primarily on the surface of the cell in a patchy distribution. Scale bar is 500 nm.

5.5 DISCUSSION

Lanthanide-binding tags (LBTs) have been used for many years now for the efficient production of fusion proteins that contain high-affinity lanthanide-binding sites [105]. These multitasking tags, which comprise only a short (<20) amino acid sequence, are easily incorporated, at the DNA level, into any recombinant protein. When complexed to a lanthanide ion, the LBT in a fusion protein provides a powerful and versatile tool to facilitate investigations involving photoluminescence [105], NMR spectroscopy [79], MRI and X-ray crystallography [106].

In this work, a new application of LBTs is described for the nanoscale imaging of proteins within cells and tissues. X-ray fluorescence microscopy is a unique and powerful method for imaging the trace element distribution, concentration, and speciation in biological cells and tissues. However, in order to be most beneficial, this information needs to be placed in the context of the subcellular organelles.

Here, the use of LBTs for XFM have been adapted, with the goal of imaging individual target proteins at <10 nm spatial resolution within biological cells and tissues while simultaneously co-localizing the trace-element distribution, concentration, and speciation. Nanoscale hard X-ray imaging has only recently been enabled by the development of third generation synchrotron sources, high-resolution nano-focusing optics [78, 79], an extremely stable environment to minimize vibrations, and stiff components to reduce thermal drift [80]. It becomes even more challenging to investigate biological specimens due to the potential for radiation-induced damage. To mitigate this, cells are often imaged in the dried or frozen-hydrated state [81]. Furthermore, since the trace elements are typically micro- to nanomolar in concentration, sensitive detectors with large solid angle are required for quantification.

In order for LBTs to be a useful protein reporter in cells and tissues, they must be detectable at low concentrations; the background signal (e.g. non-specific binding) must be minimized; and the tag must not interfere with the biological function of the cells. Here, it was shown that LBTs can be visualized on the surface of individual cells by fusing to a membrane protein, OmpA. In the regime of membrane proteins, OmpA is quite abundant at a copy number of 100,000 per cell [107]. However, in the context of the whole cell, this represents an impressive detection sensitivity that is sub-picomolar.

For intracellular proteins, the detection sensitivity is also dependent upon the transport of the lanthanide ions into the cells. To date, it is still unclear how lanthanide ions are transported into cells. At high concentrations, they are known to affect cell signaling by displacing Ca^{2+} and can promote apoptosis in cell lines by increasing the concentrations of reactive oxygen species [108]. But transport into the cell typically takes place via internalization mechanisms such as phagocytosis, endocytosis, and pinocytosis [109]. In this study, examination of the dLBT-Ubiquitin XFM images shows that lanthanide ions are transported into the cells with very low cell toxicity. However, the uptake efficiency was <20%, which could be improved.

Ubiquitin is abundant in cells and acts as a post-translational modifier that regulates a wide variety of biological processes. It exists at a concentration of ~85 µM in both free and conjugated species in cells [110]. Hence, the results shown here indicate that LBTs can be used as a reporter for proteins in the cytosol that fall in the nano- to micromolar level.

Lastly, it was important to show that the lanthanides only bind to the LBTs and do not bind non-specifically in the cells. For ubiquitin, no evidence of lanthanide uptake was observed in the cells that lacked the LBT. For OmpA, the lanthanide did not associate with other surface proteins in the control cells. However, in the LBT-OmpA cells, a small amount of lanthanide was

observed inside the cells, in addition to the cell surface. As a porin-like integral membrane protein [107], it is possible that OmpA itself helped to transport the lanthanide into the cell and/or a small amount of uptake could have occurred through internalization mechanisms.

5.6 CONCLUSIONS

In summary, lanthanide-binding tags (LBTs) were used as a GFP-like analog for 2D and 3D nanoscale imaging with X-rays. The LBTs are short peptides (15-20 amino acids) comprised of a nanomolar-affinity lanthanide-binding domain. The high affinity of the LBTs for lanthanides means that experiments can be performed at low concentrations that mitigate toxic effects. The LBTs can be easily incorporated into the target protein sequence, and their small size minimizes any deleterious effects on target protein expression, function, or transport within the cell. Here the successful demonstration of X-ray imaging of two LBT-protein conjugates, a membrane protein (OmpA) and a cytosolic protein (ubiquitin) at a 3D spatial resolution of 20 nm and a sub-picomolar detection sensitivity. Since the conjugation of LBTs and proteins follow standard molecular biology protocols, it is proposed that XFM with LBTs could become a widespread tool for 3D imaging of individual proteins within cells with a high spatial resolution while simultaneously obtaining trace element distribution.

CHAPTER 6

DISCUSSION, CONCLUSIONS, AND OUTLOOK

6.1 DISCUSSION

Although chemical fertilizers have played a very important role in providing essential nutrients like nitrates, sulfates and phosphates for trees and crops, its overuse in growing plants has resulted in several problems including a decline in soil fertility, chemical leaching into water systems and the impairment of fish and other aquatic life. The decline in soil fertility experienced by overusing chemical fertilizers hampers the growth of beneficial soil microbes, resulting in the need to use pesticides to ward off harmful fungi and microbes therefore limiting the opportunity to generate healthy soils. Additionally, chemical fertilizers are expensive and in some cases, are limited resources. Therefore, it is necessary to invest in new methods to produce healthy soils for future crop production and forest conservation. It is estimated that there are c. 50 000 fungal species that form mycorrhizal associations with c. 250 000 plant species" [29]. Mycorrhizal fungi play a key role in the cycling of carbon (C), nitrogen (N), and phosphorus (P) in ecosystems and is therefore important for global nutrient cycling. According to Sanders et al, 'up to 80% of plant N and P is provided by mycorrhizal fungi and many plant species depend on these symbionts for growth and survival'. Because mycorrhizal fungi can supply plants with nutrients that would remain 'untappable', they are vital resources for growing plants sustainably. However, the lack of understanding of this symbiotic relationship has hindered its use on large industrial scales. Acquiring spatio-chemical information about the plant and its fungal partner in situ in the soil has remained elusive because of a lack of suitable techniques. In this research, FTIR-Imaging was employed to measure an experimental system that houses a mini-ecosystem

(plant, fungi, and bacteria) to better understand the nitrogen distribution in the rhizosphere of a mycorrhizal relationship (**Specific Aim 1**). This experimental system is valuable because it provides an opportunity to image nutrient changes in the plant rhizosphere 'in situ' for the first time with FTIR-I. Furthermore, it is advantageous because of the flexibility it affords to expand the system if needed, for example, adding more than one fungal strain.

Because the nitrate infrared stretching vibration and the ammonium infrared bending vibration do not appear as distinct, non-overlapping peaks in the average infrared spectrum of the experimental system, multi-variate analysis was needed to analyze the data to predict the nutrient concentrations in the rhizosphere. (**Specific aim 2**). By using Partial Least Squares Regression (PLS-R), two quantitative predictive models (one for ammonium and one for nitrate) were generated to calculate the nitrate and ammonium concentration from FTIR spectra collected from the experimental system under different growth conditions. The quantitative models were built and validated using reference spectra measured from the growth media at different ammonium and nitrate concentrations.

To investigate the role of each symbiotic partner in the eco-system, plants were grown either independently or with a symbiotic bacterial strain or with a mycorrhizal fungus or both the symbiotic bacteria and fungus species. Results indicated the importance of growing the plant with the mycorrhizal fungi; the combined system assimilated approximately three times as much nitrate (60 mM) than the plant only system (20 mM nitrate) when grown in the control nitrate concentration in the rhizosphere. Adding the mycorrhizal fungus to the plant when grown in a low nitrate concentration resulted in a nitrate assimilation that was as much as two times the amount of nitrate than the plant only system. In fact, the nitrate concentration in the plant only system remained mostly constant indicating the plant's inefficiency to acquire nitrate in low

nitrate soils. Changes in the nitrate concentration were only visible in the first 500 μm away from the plant's root while it extended to 1500 μm, when the fungus was added indicating a larger area of soil explored by the fungus.

Although both ammonium and nitrate were provided in the growth media, the 'plant and fungus' system consumed ammonium and assimilated nitrate in both the control and low N growth media. In the control N media, ~360% of the nitrate is assimilated by the mycorrhizal fungi while 214% is assimilated in the low N growth media. In low N conditions, about 40% of the control concentration of NH_4 is consumed. This percentage is greater than the amount of NH_4 consumed in the control concentration which is approximately 10%. Although the N concentration is ¼ times the control concentration, NO_3 is still assimilated while NH_4 is being consumed despite the 1:3 (NH_4: NO_3) ratio. These trends demonstrate that NH_4 is the preferred source for consumption in the 'plant and fungus' system in both high and low N conditions. These results highlight the importance of mycorrhizal fungi in sequestering nitrogen from inorganic N sources in the rhizosphere. It has been estimated that approximately 50-70% of the nitrogen added to the soil for the plant is lost [64]. This means that most of the nitrogen is lost in the field results in water and soil pollution. Incorporating mycorrhizal fungi would enable the acquisition of these N sources that would otherwise be lost in the soil. For a plant to make the best use of nutrients in the soil it must adapt to changing environmental nutrient conditions by expressing different transporter proteins [68]. Likewise, in a mycorrhizal interaction with plant and fungi, specific transporter and receptor proteins must be expressed to transport nutrients across the apoplast, which is a zone separating the plant and fungal compartments where nutrient exchange takes place. By tagging specific nitrate and ammonium transporter proteins with lanthanide binding tags, their role in nutrient transport in a mycorrhizal relationship can be

investigated using x-ray fluorescence microscopy by measuring the lanthanide ions. In such a study, the activity of the protein could be probed with different concentrations of the corresponding ligands, example NO_3^- or NH_4^+. Such a tool would enable symbiotic organisms expressing the proteins of interest to be visualized in the rhizosphere, under different N conditions. This would provide answers to several questions example, where are the bacteria located on plant roots? What kind of protein profile gets turned on in different zones in the rhizosphere? How variable are these protein profiles in the context of microbial communities and ecological niches due to different external N environments?

To test the functionality of the LBTs for protein identification, an outer membrane protein (OmpA) and a cytosolic protein (Ubiquitin) were both tagged with the LBT in *E. coli* cells and measured with XFM. The successful X-ray imaging of the two LBT-protein conjugates were demonstrated at a 3D spatial resolution of 20 nm and a sub-picomolar detection sensitivity. The results showed that Eu was most highly concentrated near the surface of the cells where the tag is located on the fusion protein whereas Eu was absent when the protein was expressed without the tag. The elemental distribution observed for Eu was different for endogenous elements like Ca and Zn. In the cells with dLBT-ubiquitin, Ca and Zn are heterogeneously distributed in the cells whereas Eu is more uniform, which is consistent with the fact that ubiquitin is expressed throughout the cell. In the absence of the LBT on the ubiquitin, there was no evidence of Eu uptake into the cells. These results indicate that lanthanide-binding tags can be used as a GFP-like analog for 2D and 3D nanoscale imaging with X-rays. Furthermore, these tags are advantageous because of their small size which minimizes deleterious effects on target protein expression, function, or transport within the cell and they have a high affinity for

lanthanides meaning that experiments can be performed at low concentrations that mitigate toxic effects.

6.2 LIMITATIONS

One of the major limitations of this study was that it only focused on imaging the nutrient distribution in the rhizosphere region of the plant and did not include the endosphere which is the region inside the plant tissue. Examining the plant endosphere is especially important in the system with the mycorrhizal fungi. ECM have three distinct structural compartments once they form their interaction with plants; two of which are found in the rhizosphere and one in the endosphere. The fungal sheath and the hyphal strands which extend from the sheath are found in the rhizosphere while the intraradical mycelium are found in the endosphere. It is believed that inorganic sources of nitrogen are transported in different chemical forms in the different structural compartments of the fungus. Because each structural compartment has a distinct role in the nutrient uptake and transport process to the plant, it is important to explore all three regions to get a complete picture of these processes.

A second limitation of this study was that the nitrogen distribution was monitored only at one growth phase of the mycorrhizal interaction, after 6-8 weeks of plant development. While this time point was important for the plant and fungus to form a healthy and thriving mycorrhizal interaction and grow big enough to observe phenotypic changes, a more detailed approach would have been to image the nitrogen distribution at several time points over the course of several weeks. This time course experiment would provide additional information in understanding the role of the mycorrhizal fungus in acquiring nitrogen from the rhizosphere at different phases of the plant growth attributed to its associated fungus interaction.

This study utilized two different nutrient concentrations in the growth media; control nitrogen (14 mM nitrate and 5 mM ammonium) and low nitrogen (2.25 mM nitrate and 1.25 mM ammonium) which is one quarter of the control concentration. This was important to observe the impact of the mycorrhizal fungus on low N concentrations in the soil. As nitrogen conditions change in the soil from low to high N or vice versa, different transporter proteins (high affinity and low affinity proteins) get expressed to accommodate those changes. To gain a broader understanding of ammonium and nitrate usage in the systems examined under different conditions, a wider N concentration range could have been incorporated. This would entail using nitrate concentrations in the 0-14 mM range and ammonium concentrations in the 0-5 mM range to represent severely low N, very low N, low N, moderate N and control N.

Finally, only one species of plant, fungus and bacteria was each monitored. To determine if the nitrogen distribution patterns observed are truly representative of mycorrhizal interactions, at least 3 to 5 fungus species should have been tested to improve the confidence level of the observations made.

6.3 CONCLUSIONS AND OUTLOOK

By incorporating mycorrhizal fungi and growth promoting bacteria into soils as biofertilizers, crops can be grown sustainably on large industrial scales. Currently, mycorrhizal relationships are not well understood and remain underutilized natural resources suitable for enhancing crop and tree production. To understand the role of mycorrhizal fungi in nitrogen uptake and transport in the rhizosphere, an experimental method suitable for growing a plant ecosystem (plant grown in combination with mycorrhizal fungi and growth promoting bacteria) and compatible with infrared imaging was developed. Poplar was chosen as the model plant in the experimental system because it is a fast growing, tall tree (up to 165 ft) which has an

extensive distribution range across North America making it suitable for the production of biomass [111]. The mycorrhizal fungus, *L. bicolor* was chosen because it forms a well-established ectomycorrhizal interaction with poplar [111]. Multivariate regression analysis was performed on the data from infrared imaging to quantitate the nitrogen changes occurring in the region near the root-the rhizosphere.

The results indicated that (1) nitrogen gradients are established in the soil to facilitate the movement of nitrogen from the soil to the plant, (2) the fungi establish a steeper gradient profile and over a longer distance away from the plant root, and (3) the nitrogen gradient is more prominent under low N conditions with the fungi suggesting that it plays an especially important role in nutrient depleted soils. Additionally, we have developed the use of lanthanide binding tags (LBT) with x-ray fluorescence microscopy to image transporters in the membranes of intact bacteria. In this application, we have shown that LBTs + XFM have the required detection sensitivity and spatial resolution to visualize single proteins in the membrane of the cell and can be used in the future to study nitrogen transporter proteins at the subcellular level. The work presented is of great potential to understanding mycorrhizal interactions and provides a technique to monitor both physical and chemical changes and can be used to predict changes in nutrient concentration on different spatial scales before implementing on a large industrial scale to grow crops.

The work presented in this thesis shows how an experimental system, compatible with infrared imaging was utilized to investigate the role of mycorrhizal fungi in the nitrogen distribution in the plant rhizosphere. This first-time approach of obtaining chemical data about nutrients like nitrate, ammonium and sucrose from an experimental system is unique and relevant to understanding changes in nutrient distribution in situ on a whole system scale. This approach

is applicable to monitoring responses to changing environments including changes in micro-organisms and or nutrients such as phosphates or sulfates, on a small scale before proceeding to large scale setups of crops and trees. The use of x-ray fluorescence microscopy to probe lanthanide binding tagged proteins provides a great tool to not only resolve transporter proteins on a high-resolution scale, ~10 nm, but to also count the number of protein copies translated under certain conditions, example when plants are grown with mycorrhizal fungi under low nutrient conditions. This is important in establishing the role of mycorrhizal fungi in the nutrient distribution and transport in the rhizosphere. While this research lays down an excellent framework for predicting nutrient concentrations in the rhizosphere, there is surely room for increasing the scope of the project investigated using this predictive model.

In the future, FTIR-I data can be collected from samples in aqueous conditions in real time at several time points for 6 to 8 weeks. In the studies performed, infrared data were collected from samples after they had been dried because of the overbearing absorbance intensities that molecular vibrations from water exhibit. By collecting data in real time from the plant samples over an eight-week period, a more detailed and accurate understanding of the mycorrhizal fungi's role in nutrient uptake and transport in the soil can be established. In such a case, small, on the order of a few hundred microns, high resolution infrared chemical maps (10 micron beam/pixel), would need to be collected away from the plant's root and over the same area each time.

In addition to the time course studies in real time, investigating the distribution of several major macronutrients including phosphorous and sulfur sources would provide a more comprehensive understanding of the role of mycorrhizal fungi in nutrient uptake, instead of only nitrogen uptake. Phosphorus is an important nutrient for plant growth but because phosphates

have very low soil solubility their concentration remains very low in the rhizosphere once used up by root hairs [112]. Sulfur is also an essential macro-nutrient for plant growth but 95% of it is available in organic forms in the soil as sulfate-esters and sulfonates that only become available to plants in inorganic forms via microbial conversion and mycorrhizal fungus transport to plants [113]. It would certainly provide a broader perspective on how one nutrient affects the other's transport in this symbiotic relationship.

To fully understand how a mycorrhizal fungus improves the nutrient uptake in the soil and improves biomass production, the role of the transporter proteins expressed in this relationship must also be investigated. Therefore, future studies aimed at understanding changes in the nutrient distribution with FTIR-I should be conducted in parallel with proteomic studies to isolate and understand the role of the proteins responsible for nutrient (nitrogen and other nutrients) transport. Once these proteins are isolated, their role in nutrient transport in the rhizosphere can be further investigated by probing with LBTs and XFM. Once accomplished, this would make it possible to extend these studies to other types of mycorrhizal fungi for example, *Glomus intraradices* which have been shown to be beneficial in phosphorus uptake [114] or growth promoting bacteria like *Rhizobium sullae which produce plant-growth promoting substances* [115] and plants to improve our understanding of these interactions for use in growing plants sustainably in low nutrient soils.

REFERENCES

1. Philippot, L., et al., *Going back to the roots: the microbial ecology of the rhizosphere.* Nature Reviews Microbiology, 2013. **11**: p. 789.
2. Bonfante, P. and A. Genre, *Mechanisms underlying beneficial plant–fungus interactions in mycorrhizal symbiosis.* Nature Communications, 2010. **1**: p. 48.
3. Premachandra, D., L. Hudek, and L. Brau, *Bacterial modes of action for enhancing of plant growth.* Journal of biotechnology & biomaterials, 2016. **6**(3): p. 1-8.
4. Gupta G, et al., *Plant Growth Promoting Rhizobacteria (PGPR): Current and Future Prospects for Development of Sustainable Agriculture.* J Microb Biochem Technology, 2015. **7**: p. 096-102.
5. Kang, Y., S. Khan, and X. Ma, *Climate change impacts on crop yield, crop water productivity and food security – A review.* Progress in Natural Science, 2009. **19**(12): p. 1665-1674.
6. Agency, U.S.E.P., *Climate Impacts on Agriculture and Food Supply.* 2016.
7. Rennenberg, H., H. Wildhagen, and B. Ehlting, *Nitrogen nutrition of poplar trees.* Plant Biol (Stuttg), 2010. **12**(2): p. 275-91.
8. Garcia, K. and S.D. Zimmermann, *The role of mycorrhizal associations in plant potassium nutrition.* Frontiers in Plant Science, 2014. **5**: p. 337.
9. Müller, T., et al., *Nitrogen transport in the ectomycorrhiza association: The Hebeloma cylindrosporum–Pinus pinaster model.* Phytochemistry, 2007. **68**(1): p. 41-51.
10. Sikes, B.A., *When do arbuscular mycorrhizal fungi protect plant roots from pathogens?* Plant Signaling & Behavior, 2010. **5**(6): p. 763-765.
11. Berruti, A., et al., *Arbuscular Mycorrhizal Fungi as Natural Biofertilizers: Let's Benefit from Past Successes.* Frontiers in Microbiology, 2015. **6**: p. 1559.
12. Popp, J., et al., *The effect of bioenergy expansion: Food, energy, and environment.* Renewable and Sustainable Energy Reviews, 2014. **32**(Supplement C): p. 559-578.
13. McKendry, P., *Energy production from biomass (part 1): overview of biomass.* Bioresource Technology, 2002. **83**(1): p. 37-46.
14. Fargione, J., et al., *Land Clearing and the Biofuel Carbon Debt.* Science, 2008. **319**(5867): p. 1235.
15. da C. Jesus, E., et al., *Bacterial Communities in the Rhizosphere of Biofuel Crops Grown on Marginal Lands as Evaluated by 16S rRNA Gene Pyrosequences.* BioEnergy Research, 2010. **3**(1): p. 20-27.
16. McNear, D., *The rhizosphere-roots, soil and everything in between*. Vol. 4. 2013.
17. Koo, B.J., et al., *ROOT EXUDATES AND MICROORGANISMS A2 - Hillel, Daniel*, in *Encyclopedia of Soils in the Environment*. 2005, Elsevier: Oxford. p. 421-428.
18. Hinsinger, P., et al., *Rhizosphere: biophysics, biogeochemistry and ecological relevance.* Plant and Soil, 2009. **321**(1): p. 117-152.
19. Yang, C.-H. and D.E. Crowley, *Rhizosphere Microbial Community Structure in Relation to Root Location and Plant Iron Nutritional Status.* Applied and Environmental Microbiology, 2000. **66**(1): p. 345-351.

20.   Service, U.S.N.R.C., *Soil Biology Primer*. 1999: U.S. Department of Agriculture, Natural Resources Conservation Service.

21.   Bücking, H., E. Liepold, and P. Ambilwade, *The Role of the Mycorrhizal Symbiosis in Nutrient Uptake of Plants and the Regulatory Mechanisms Underlying These Transport Processes*, in *Plant Science*, N.K. Dhal and S.C. Sahu, Editors. 2012, InTech: Rijeka. p. Ch. 04.

22.   Aspray, T.J., et al., *Mycorrhization helper bacteria: a case of specificity for altering ectomycorrhiza architecture but not ectomycorrhiza formation.* Mycorrhiza, 2006. **16**(8): p. 533-541.

23.   Panpatte, D.G., et al., *Pseudomonas fluorescens: A Promising Biocontrol Agent and PGPR for Sustainable Agriculture*, in *Microbial Inoculants in Sustainable Agricultural Productivity: Vol. 1: Research Perspectives*, D.P. Singh, H.B. Singh, and R. Prabha, Editors. 2016, Springer India: New Delhi. p. 257-270.

24.   de Souza, R., A. Ambrosini, and L.M.P. Passaglia, *Plant growth-promoting bacteria as inoculants in agricultural soils.* Genetics and Molecular Biology, 2015. **38**(4): p. 401-419.

25.   Chrispeels MJ, C.N., Schroeder JI., *Proteins for transport of water and mineral nutrients across the membranes of plant cells.* The Plant Cell, 1999. **11**(4): p. 661-76.

26.   Nath, B., *Environmental management in practice. Volume 2 Volume 2*. 1999, London: Routledge.

27.   Hayat, R., et al., *Soil beneficial bacteria and their role in plant growth promotion: a review.* Annals of Microbiology, 2010. **60**(4): p. 579-598.

28.   Paungfoo-Lonhienne, C., et al., *Plants can use protein as a nitrogen source without assistance from other organisms.* Proceedings of the National Academy of Sciences of the United States of America, 2008. **105**(11): p. 4524-4529.

29.   van der Heijden, M.G.A., et al., *Mycorrhizal ecology and evolution: the past, the present, and the future.* New Phytologist, 2015. **205**(4): p. 1406-1423.

30.   Roose, T., et al., *Challenges in imaging and predictive modeling of rhizosphere processes.* Plant and Soil, 2016. **407**(1): p. 9-38.

31.   Cseke, L., Kirakosyan, A. , Kaufman, P. , Westfall, M. , *Handbook of Molecular and Cellular Methods in Biology and Medicine, Third Edition*. 2012: Boca Raton: CRC Press.

32.   Miller, L.M. and P. Dumas, *From structure to cellular mechanism with infrared microspectroscopy.* Current Opinion in Structural Biology, 2010. **20**(5): p. 649-656.

33.   Chen, S., et al., *The Bionanoprobe: hard X-ray fluorescence nanoprobe with cryogenic capabilities.* Journal of Synchrotron Radiation, 2014. **21**(Pt 1): p. 66-75.

34.   Yan, H. and Y.S. Chu, *Optimization of multilayer Laue lenses for a scanning X-ray microscope.* Journal of Synchrotron Radiation, 2013. **20**(1): p. 89-97.

35.   Midgley, P.A., et al., *Nanotomography in the chemical, biological and materials sciences.* Chemical Society Reviews, 2007. **36**(9): p. 1477-1494.

36.   O'Gara, F., D.N. Dowling, and B. Boesten, *Molecular Ecology of Rhizosphere Microorganisms: Biotechnology and the Release of GMOs*. 2008: Wiley.

37.   Zuccaro, A., U. Lahrmann, and G. Langen, *Broad compatibility in fungal root symbioses.* Current Opinion in Plant Biology, 2014. **20**(0): p. 135-145.

38.   Cruz, A.F. and T. Ishii, *Arbuscular mycorrhizal fungal spores host bacteria that affect nutrient biodynamics and biocontrol of soil-borne plant pathogens.* Biology Open, 2012. **1**(1): p. 52-57.

39. Clode, P.L., et al., *In Situ Mapping of Nutrient Uptake in the Rhizosphere Using Nanoscale Secondary Ion Mass Spectrometry.* Plant Physiology, 2009. **151**(4): p. 1751-1757.

40. Sun, Y., et al., *Optimizing detector geometry for trace element mapping by X-ray fluorescence.* Ultramicroscopy, 2015. **152**: p. 44-56.

41. Zhao, F.-J., et al., *Imaging element distribution and speciation in plant cells.* Trends in Plant Science, 2014. **19**(3): p. 183-192.

42. Larsen, P.E., et al., *Using next generation transcriptome sequencing to predict an ectomycorrhizal metabolome.* BMC Systems Biology, 2011. **5**(1): p. 1-14.

43. Larsen, P.E., et al., *Using deep RNA sequencing for the structural annotation of the Laccaria bicolor mycorrhizal transcriptome.* PLoS One, 2010. **5**.

44. Lloyd, G. and B. McCown, *Commercially-feasible micropropagation of mountain laurel, Kalmia latifolia, by use of shoot-tip culture.* Combined Proceedings, International Plant Propagators' Society, 1980. **30**: p. 421-427.

45. Park, J.K., T. Khan, and J.Y. Jung, *Structural studies of the glucuronic acid oligomers produced by Gluconacetobacter hansenii strain.* Carbohydrate Polymers, 2006. **63**(4): p. 482-486.

46. Tewari, J. and J. Irudayaraj, *Quantification of Saccharides in Multiple Floral Honeys Using Fourier Transform Infrared Microattenuated Total Reflectance Spectroscopy.* Journal of Agricultural and Food Chemistry, 2004. **52**(11): p. 3237-3243.

47. Wang, J., et al., *Rapid Analysis of Glucose, Fructose, Sucrose, and Maltose in Honeys from Different Geographic Regions using Fourier Transform Infrared Spectroscopy and Multivariate Analysis.* Journal of Food Science, 2010. **75**(2): p. C208-C214.

48. Cseke, L.J., S.B. Cseke, and G.K. Podila, *High efficiency poplar transformation.* Plant Cell Reports, 2007. **26**(9): p. 1529-1538.

49. Jastrzębski, W., et al., *Infrared spectroscopy of different phosphates structures.* Spectrochimica Acta Part A: Molecular and Biomolecular Spectroscopy, 2011. **79**(4): p. 722-727.

50. Goebbert, D.J., et al., *Infrared Spectroscopy of the Microhydrated Nitrate Ions $NO_3^-(H_2O)_{1-6}†$.* The Journal of Physical Chemistry A, 2009. **113**(26): p. 7584-7592.

51. Lane, M.D., *Mid-infrared emission spectroscopy of sulfate and sulfate-bearing minerals.* American Mineralogist. **92**(1): p. 1-18.

52. Kuhn, L.P., *Infrared Spectra of Carbohydrates.* Analytical Chemistry, 1950. **22**(2): p. 276-283.

53. Ahmed, A.B.A., et al., *The Role of the Mycorrhizal Symbiosis in Nutrient Uptake of Plants and the Regulatory Mechanisms Underlying These Transport Processes*. 2012: INTECH Open Access Publisher.

54. Behie, S.W. and M.J. Bidochka, *Nutrient transfer in plant–fungal symbioses.* Trends in Plant Science. **19**(11): p. 734-740.

55. Bücking, H. and A. Kafle, *Role of Arbuscular Mycorrhizal Fungi in the Nitrogen Uptake of Plants: Current Knowledge and Research Gaps.* Agronomy, 2015. **5**(4).

56. Vargas, W.A., J.C. Mandawe, and C.M. Kenerley, *Plant-Derived Sucrose Is a Key Element in the Symbiotic Association between Trichoderma virens and Maize Plants.* Plant Physiology, 2009. **151**(2): p. 792-808.

57. Kraiser, T., et al., *A holistic view of nitrogen acquisition in plants.* Journal of Experimental Botany, 2011. **62**(4): p. 1455-1466.

58. Richardson, A., et al., *Acquisition of phosphorus and nitrogen in the rhizosphere and plant growth promotion by microorganisms.* Plant and Soil, 2009. **321**(1-2): p. 305-339.

59. Chamam, A., et al., *Plant secondary metabolite profiling evidences strain-dependent effect in the Azospirillum–Oryza sativa association.* Phytochemistry, 2013. **87**(0): p. 65-77.

60. Miller, A., *Plant Nitrogen Nutrition and Transport.* In: eLS, May 2010.

61. Nehls, U., et al., *Fungal carbohydrate support in the ectomycorrhizal symbiosis: a review.* Plant Biology, 2010. **12**(2): p. 292-301.

62. Fellbaum, C.R., et al., *Carbon availability triggers fungal nitrogen uptake and transport in arbuscular mycorrhizal symbiosis.* Proceedings of the National Academy of Sciences, 2012. **109**(7): p. 2666-2671.

63. Stavitski, E., et al., *Dynamic full-field infrared imaging with multiple synchrotron beams.* Analytical chemistry, 2013. **85**(7): p. 3599-3605.

64. Masclaux-Daubresse, C., et al., *Nitrogen uptake, assimilation and remobilization in plants: challenges for sustainable and productive agriculture.* Annals of Botany, 2010. **105**(7): p. 1141-1157.

65. Jones, D.L., et al., *Competition between plant and bacterial cells at the microscale regulates the dynamics of nitrogen acquisition in wheat (Triticum aestivum).* The New Phytologist, 2013. **200**(3): p. 796-807.

66. *Chapter 14 A Source of Inorganic Nutrients and Microbial Food*, in *Developments in Soil Science*, F.E. Allison, Editor. 1973, Elsevier. p. 277-300.

67. Victor, T., et al., *Imaging Nutrient Distribution in the Rhizosphere Using FTIR Imaging.* Analytical Chemistry, 2017. **89**(9): p. 4831-4837.

68. Krapp, A., *Plant nitrogen assimilation and its regulation: a complex puzzle with missing pieces.* Current Opinion in Plant Biology, 2015. **25**(Supplement C): p. 115-122.

69. Govindarajulu, M., et al., *Nitrogen transfer in the arbuscular mycorrhizal symbiosis.* Nature, 2005. **435**: p. 819.

70. Tischner, R., *Nitrate uptake and reduction in higher and lower plants.* Plant, Cell & Environment, 2000. **23**(10): p. 1005-1024.

71. Kashiv, Y., et al., *Imaging trace element distributions in single organelles and subcellular features.* 2016. **6**: p. 21437.

72. Fahrni, C.J., *Biological applications of X-ray fluorescence microscopy: exploring the subcellular topography and speciation of transition metals.* Current Opinion in Chemical Biology, 2007. **11**(2): p. 121-127.

73. de Jonge, M.D. and S. Vogt, *Hard X-ray fluorescence tomography—an emerging tool for structural visualization.* Current Opinion in Structural Biology, 2010. **20**(5): p. 606-614.

74. Yan, H., et al., *Multimodality hard-x-ray imaging of a chromosome with nanoscale spatial resolution.* 2016. **6**: p. 20112.

75. de Jonge, M.D., et al., *Quantitative 3D elemental microtomography of Cyclotella meneghiniana at 400-nm resolution.* Proceedings of the National Academy of Sciences, 2010. **107**(36): p. 15676-15680.

76. Punshon, T., M.L. Guerinot, and A. Lanzirotti, *Using synchrotron X-ray fluorescence microprobes in the study of metal homeostasis in plants.* Annals of Botany, 2009. **103**(5): p. 665-672.

77. Chaffey, N., *Alberts, B., Johnson, A., Lewis, J., Raff, M., Roberts, K. and Walter, P. Molecular biology of the cell. 4th edn.* Annals of Botany, 2003. **91**(3): p. 401-401.

78. Huang, X., et al., *11 nm hard X-ray focus from a large-aperture multilayer Laue lens.* 2013. **3**: p. 3562.

79. Morgan, A.J., et al., *High numerical aperture multilayer Laue lenses.* 2015. **5**: p. 9892.

80. Nazaretski, E., et al., *Pushing the limits: an instrument for hard X-ray imaging below 20 nm.* Journal of Synchrotron Radiation, 2015. **22**(2): p. 336-341.

81. Nam, D., et al., *Imaging Fully Hydrated Whole Cells by Coherent X-Ray Diffraction Microscopy.* Physical Review Letters, 2013. **110**(9): p. 098103.

82. Kim, S.A., et al., *Localization of iron in Arabidopsis seed requires the vacuolar membrane transporter VIT1.* Science, 2006. **314**(5803): p. 1295-8.

83. Yamamoto, Y. and K. Shinohara, *Application of X-ray microscopy in analysis of living hydrated cells.* The Anatomical Record, 2002. **269**(5): p. 217-223.

84. Robinson, I. and X. Huang, *X-ray imaging: Reaching the third dimension.* Nat Mater, 2017. **16**(2): p. 160-161.

85. Deng, J., et al., *X-ray ptychographic and fluorescence microscopy of frozen-hydrated cells using continuous scanning.* Scientific Reports, 2017. **7**(1): p. 445.

86. Li, L., et al. *PyXRF: Python-based X-ray fluorescence analysis package*. in *SPIE Optical Engineering + Applications*. 2017. SPIE.

87. Gürsoy, D., et al. *TomoPy: A framework for the analysis of synchrotron tomographic data*. in *SPIE Optical Engineering + Applications*. 2014. SPIE.

88. Hensley, M.P., D.L. Tierney, and M.W. Crowder, *Zn(II) binding to E. coli 70S Ribosomes.* Biochemistry, 2011. **50**(46): p. 9937-9939.

89. Blindauer, C.A., *Advances in the molecular understanding of biological zinc transport.* Chemical Communications, 2015. **51**(22): p. 4544-4563.

90. Takahashi, H., et al., *The dynamic balance of import and export of zinc in Escherichia coli suggests a heterogeneous population response to stress.* Journal of The Royal Society Interface, 2015. **12**(106).

91. Bakshi, S., et al., *Superresolution Imaging of Ribosomes and RNA Polymerase in Live Escherichia coli Cells.* Molecular Microbiology, 2012. **85**(1): p. 21-38.

92. Chai, Q., et al., *Organization of Ribosomes and Nucleoids in Escherichia coli Cells during Growth and in Quiescence.* Journal of Biological Chemistry, 2014. **289**(16): p. 11342-11352.

93. Dillon, S.C. and C.J. Dorman, *Bacterial nucleoid-associated proteins, nucleoid structure and gene expression.* Nat Rev Micro, 2010. **8**(3): p. 185-195.

94. Bakshi, S., H. Choi, and J.C. Weisshaar, *The spatial biology of transcription and translation in rapidly growing Escherichia coli.* Frontiers in Microbiology, 2015. **6**(636).

95. Ma, Z., F.E. Jacobsen, and D.P. Giedroc, *Metal Transporters and Metal Sensors: How Coordination Chemistry Controls Bacterial Metal Homeostasis.* Chemical reviews, 2009. **109**(10): p. 4644-4681.

96. Silhavy, T.J., D. Kahne, and S. Walker, *The Bacterial Cell Envelope.* Cold Spring Harbor Perspectives in Biology, 2010. **2**(5): p. a000414.

97. Djoko, K.Y., et al., *The Role of Copper and Zinc Toxicity in Innate Immune Defense against Bacterial Pathogens.* The Journal of Biological Chemistry, 2015. **290**(31): p. 18954-18961.

98. Paunesku, T., et al., *X-ray fluorescence microprobe imaging in biology and medicine.* Journal of Cellular Biochemistry, 2006. **99**(6): p. 1489-1502.

99. Chen, S., et al., *The Bionanoprobe: hard X-ray fluorescence nanoprobe with cryogenic capabilities.* J Synchrotron Radiat, 2014. **21**(Pt 1): p. 66-75.

100. Malasics, A., et al., *Simulations of calcium channel block by trivalent cations: Gd(3+) competes with permeant ions for the selectivity filter.* Biochimica et biophysica acta, 2010. **1798**(11): p. 2013-2021.

101. H Lecker, S., A. Goldberg, and W. Mitch, *Protein Degradation by the Ubiquitin-Proteasome Pathway in Normal and Disease States*. Vol. 17. 2006. 1807-19.

102. Reynolds, A.M., B.R. Sculimbrene, and B. Imperiali, *Lanthanide-Binding Tags with Unnatural Amino Acids: Sensitizing Tb3+ and Eu3+ Luminescence at Longer Wavelengths.* Bioconjugate Chemistry, 2008. **19**(3): p. 588-591.

103. Peacock, A.F.A., *Chapter Twenty-Four - De Novo Designed Imaging Agents Based on Lanthanide Peptides Complexes*, in *Methods in Enzymology*, V.L. Pecoraro, Editor. 2016, Academic Press. p. 557-580.

104. Arora, A., et al., *Refolded outer membrane protein A of Escherichia coli forms ion channels with two conductance states in planar lipid bilayers.* J Biol Chem, 2000. **275**(3): p. 1594-600.

105. Allen, K.N. and B. Imperiali, *Lanthanide-tagged proteins--an illuminating partnership.* Curr Opin Chem Biol, 2010. **14**(2): p. 247-54.

106. Martin, L., *Development of lanthanide-binding tags (LBTs) as powerful and versatile peptides for use in studies of proteins and protein interactions*. 2008.

107. Parent, K.N., et al., *OmpA and OmpC are critical host factors for bacteriophage Sf6 entry in Shigella.* Molecular microbiology, 2014. **92**(1): p. 47-60.

108. Skovran, E. and N.C. Martinez-Gomez, *Just add lanthanides.* Science, 2015. **348**(6237): p. 862.

109. Cheng, Y., et al., *The transport kinetics of lanthanide species in a single erythrocyte probed by confocal laser scanning microscopy.* J Biol Inorg Chem, 1999. **4**(4): p. 447-56.

110. Kaiser, S.E., et al., *Protein standard absolute quantification (PSAQ) method for the measurement of cellular ubiquitin pools.* Nature methods, 2011. **8**(8): p. 691-696.

111. Müller, A., et al., *Growing poplars for research with and without mycorrhizas.* Frontiers in Plant Science, 2013. **4**: p. 332.

112. Smith, S.E., et al., *Roles of Arbuscular Mycorrhizas in Plant Phosphorus Nutrition: Interactions between Pathways of Phosphorus Uptake in Arbuscular Mycorrhizal Roots Have Important Implications for Understanding and Manipulating Plant Phosphorus Acquisition.* Plant Physiology, 2011. **156**(3): p. 1050.

113. Gahan, J. and A. Schmalenberger, *The role of bacteria and mycorrhiza in plant sulfur supply.* Frontiers in Plant Science, 2014. **5**: p. 723.

114. Banerjee, K., et al., *Screening of efficient arbuscular mycorrhizal fungi for Azadirachta indica under nursery condition: a step towards afforestation of semi-arid region of western India.* Brazilian Journal of Microbiology, 2013. **44**: p. 587-594.

115. Chiboub, M., et al., *Characterization of efficient plant-growth-promoting bacteria isolated from Sulla coronaria resistant to cadmium and to other heavy metals.* Comptes Rendus Biologies, 2016. **339**(9): p. 391-398.